

1

[ATLAS Semivisible Jets]

2

[Elena Laura Busch]

3

Submitted in partial fulfillment of the
requirements for the degree of
Doctor of Philosophy
under the Executive Committee
of the Graduate School of Arts and Sciences

4

5

6

7

8

COLUMBIA UNIVERSITY

9

2024

10

© 2024

11

[Elena Laura Busch]

12

All Rights Reserved

13

Abstract

14

[ATLAS Semivisible Jets]

15

[Elena Laura Busch]

16

Abstract of dissertation (place-holder).

Table of Contents

18	Acknowledgments	vii
19	Dedication	viii
20	Introduction or Preface	1
21	Chapter 1: The Standard Model	2
22	1.1 Phenomenology: Particles and Forces	2
23	1.1.1 Particles	2
24	1.1.2 Forces	3
25	1.2 QCD and Jets	6
26	1.3 Symmetries	7
27	1.3.1 Spontaneous Symmetry Breaking and The Higgs Mechanism	8
28	1.4 Experimental Validation of the Standard Model	9
29	1.5 Limitations of the Standard Model	10
30	Chapter 2: Physics Beyond the Standard Model	12
31	2.1 Hidden Valley Models	12
32	2.2 Dark QCD	13
33	2.3 Semi-visible Jets	14

34	Chapter 3: The Large Hadron Collider	16
35	3.1 Accelerator Physics	17
36	3.1.1 The Journey of a Proton	17
37	3.1.2 Magnets	18
38	3.2 Luminosity	19
39	3.3 LHC Timeline	22
40	Chapter 4: The ATLAS Detector	24
41	4.1 Coordinate System and Geometry	24
42	4.2 Inner Detector	26
43	4.2.1 Pixel Detector	26
44	4.2.2 Semiconductor Tracker	27
45	4.2.3 Transition Radiation Tracker	27
46	4.3 Calorimeters	28
47	4.3.1 Liquid Argon Calorimeter	29
48	4.3.2 Tile Calorimeter	32
49	4.4 Muon Spectrometer	33
50	4.5 Magnet System	35
51	4.6 Forward Detectors	36
52	4.7 Trigger and Data Acquisition	37
53	Chapter 5: Particle Reconstruction and Identification	39
54	5.1 Inner Detector Tracks	39
55	5.2 Photons and Electrons	40

56	5.3 Muons	42
57	5.4 Jets	44
58	5.4.1 Calorimeter Clusters	45
59	5.4.2 Particle Flow Algorithm	46
60	5.4.3 Jet Clustering	47
61	5.4.4 Ghost Track Association	50
62	5.5 Missing Transverse Energy	51
63	Conclusion or Epilogue	53
64	References	57
65	Appendix A: Experimental Equipment	62
66	Appendix B: Data Processing	63

List of Figures

68	1.1	Diagram of the 17 particles comprising the Standard Model	3
69	1.2	Fundamental particle interactions of the three fundamental forces described by the	
70		Standard Model [2].	5
71	1.3	An example Feynmann diagram of jet production	6
72	1.4	An illustration of the “hat shaped” potential of the Higgs field, resulting in a non-	
73		zero vacuum expectation value.	8
74	2.1	Illustration of the hidden valley potential	13
75	2.2	The massive mediator particle Z' of the s-channel realization of a HV model . . .	13
76	3.1	The LHC accelerator complex at CERN [27]	18
77	3.2	The octants of the LHC and location of various beam activities [26]. Stars indicate	
78		the locations of beam collisions, and the associated detectors recording the	
79		outcome of those collisions.	19
80	3.3	(Left) Total integrated luminosity over the course of Run 2. (Right) Average num-	
81		ber of pp interactions per bunch crossing in Run 2. Each curve is weighted by the	
82		integrated luminosity for the year.	21
83	3.4	Timeline of LHC and HL-LHC activities [29]. Integrated luminosity estimates are	
84		approximate, and not reflective of the exact amount delivered to each experiment. .	23
85	4.1	ATLAS coordinate system and geometry	26
86	4.2	A 3D visualization of the structure of the ID in the barrel region [33]	27
87	4.3	ATLAS calorimetery system [34]	28

88	4.4	Diagram of a segment of the EMB, demonstrating the accordion plate arrangement [35]	30
90	4.5	A LAr pulse as produced in the detector (triangle) and after shaping (curve) [35]	31
91	4.6	Readout gap structure in HEC [35]	31
92	4.7	TileCal wedge module [38]	33
93	4.8	Cross section view of the muon spectrometer system [39]	34
94	4.9	Layout of the barrel and endcap toroid magnets [32]	36
95	5.1	Graphic illustrating the various objects and high level features identified by ATLAS object reconstruction, and their interaction with different systems of the ATLAS detector [42]	40
98	5.2	Track reconstruction seeding, finding and fitting illustration [43]	41
99	5.3	Three types of EM object candidates [45].	42
100	5.4	Four types of muon track candidates [47].	44
101	5.5	The fragmentation and hadronization processes undergone by a quark produced in a proton-proton collision [49].	45
103	5.6	A flow chart illustrating the particle flow algorithm progression [54].	48
104	5.7	A comparison of jet clustering with four different jet algorithms. The anti- k_t algorithm is observed to create the most conical jets, where the shape of the jet is immune to the presence of soft radiation [50].	49
107	5.8	A comparison of MC simulation and data for $Z \rightarrow \mu\mu$ events where real $E_T^{\text{miss}} = 0$ [61]. The resolution of the missing energy in the transverse ($x - y$) plane is observed to increase with increasing total $\sum E_T$	52

List of Tables

111

Acknowledgements

112 Insert your acknowledgements text here. This page is optional, you may delete it if not
113 needed.

114

Dedication

115

Dedicated to my friends and family

116

Introduction or Preface

117 Insert your preface text here if applicable. This page is optional, you may delete it if not
118 needed. If you delete this page make sure to move page counter comment in thesis.tex to correct
119 location.

Chapter 1: The Standard Model

122 The Standard Model of particle physics is a universally accepted framework which explains
 123 the interactions of fundamental particles. All known fundamental particles, outlined in Figure
 124 1.1, are represented in the Standard Model. The model describes three of the four known forces:
 125 the electromagnetic force, the weak force, and the strong force. Gravity, the fourth fundamental
 126 force, is not addressed by the Standard Model. The Standard Model was primarily developed over
 127 the course of the 1960s and 1970s, by combining the work of many physicists into one coherent
 128 model. The Standard Model has been established as a well-tested theory by decades of experimen-
 129 tal physics research.

130 This chapter will seek to introduce the phenomenology and mathematical foundations of the
 131 Standard Model, and present the supporting experimental evidence. Phenomenon which are unex-
 132 plained by the Standard Model such as gravity will be considered at the end of the chapter, leading
 133 to an exploration of theories beyond the Standard Model in the subsequent chapter.

134 **1.1 Phenomenology: Particles and Forces**

135 **1.1.1 Particles**

136 A classic representation of the particles comprising the Standard Model is shown in Figure
 137 1.1. The two primary particles classes are bosons (gauge bosons and the scalar Higgs boson) and
 138 fermions (leptons and quarks). The bosons are carriers of fundamental forces, while the fermions
 139 are the building blocks of matter. Fermions are sorted into three *generations*, and each fermion is
 140 identified by a unique *flavor*.

141 Each entry in the table in Figure 1.1 is accompanied by 3 characteristic numbers: mass, charge,
 142 and spin. The mass of each particle is determined to limited precision by experimental observa-

Standard Model of Elementary Particles

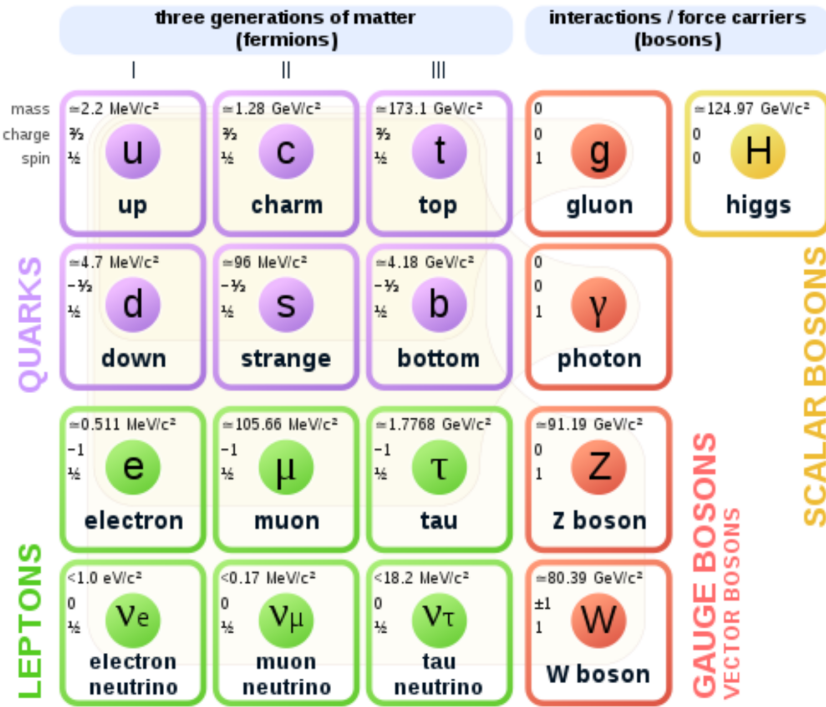


Figure 1.1: Diagram of the 17 particles comprising the Standard Model

143 tion, with the exception of photons and gluons which are known to be massless. Charge refers to
 144 the electromagnetic charge in the case of leptons and W bosons, and to color charge in the case
 145 of quarks and gluons. Spin is an intrinsic form of angular momentum carried by fundamental
 146 particles; all fermions have half integer spin, while bosons have integer spin.

147 Each particle is also known to have an *antiparticle*. Each antiparticle has the same mass but the
 148 opposite charge of their Standard Model counter part; for example, the antiparticle of the electron
 149 is the positron, which has all the same properties but a positive charge. The photon, Z boson,
 150 and Higgs are each their own antiparticle. The nature of antineutrinos is an open question driving
 151 neutrino physics research, as it is not currently known whether neutrinos are their own antiparticle.

1.1.2 Forces

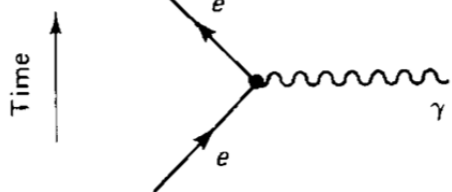
153 The three fundamental forces explained by the Standard Model are the electromagnetic force,
 154 the strong force, and the weak force. The photon is the carrier of the electromagnetic force, which

155 dictates the nature of interactions between electrically charged particles, and is widely covered by
156 introductory physics courses. The electromagnetic force has an infinite interaction range, a result
157 of the massless and non-self interaction nature of the photon. The electromagnetic interaction is
158 described by the theory of quantum electrodynamics (QED).

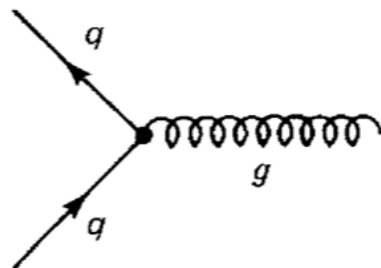
159 The weak force gives rise to atomic radiation and decay. It allows for the processes of beta
160 decay, which enables conversion between neutrons and protons within the nucleus of an atom. In
161 the process of beta decay, a proton decays into a neutron, a positron, and a neutrino; or, a neutron
162 decays into a proton, an electron and an antineutrino. The weak interaction allows for quark flavor
163 mixing, the which enables beta decay. The W^+ , W^- , and Z^0 are the force carriers of the weak force.
164 The effective range of the weak force is limited to subatomic distances, as a result of the massive
165 nature of the mediator bosons. The unified theory of the electroweak interaction posits that at high
166 enough energies the electromagnetic interaction and the weak force merge into the same force.
167 This threshold is termed the unification energy and calculated to be about 246 GeV [1].

168 The strong force confines quarks into hadron particles, such as protons and neutrons. The
169 strong force also allows for the creation of atomic nuclei by binding protons and neutrons together,
170 and is generally referred to as the “nuclear force” in this context. The gluon is the mediator of
171 the strong force, which is a short-range force which acts at subatomic distances on the order of
172 10^{-15} m. At this range, the strong force is about 100x as strong as the electromagnetic force,
173 which allows for the creation of positively charged nuclei [2]. The strong force is described by the
174 theory of quantum chromodynamics (QCD). In the same way that QED dictates the interaction of
175 electrically charges particles, QCD dictates the interactions of *color-charged* particles. Due to the
176 particular importance of QCD in this thesis, this topic will be explored in detail in section 1.2.

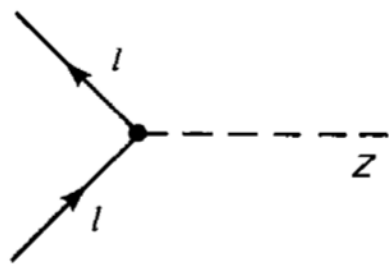
177 The fundamental Feynmann diagram for each of the three forces discussed here is depicted
178 in Figure 1.2. The fourth fundamental force, gravity, is not currently explained by any known
179 mechanism within the Standard Model.



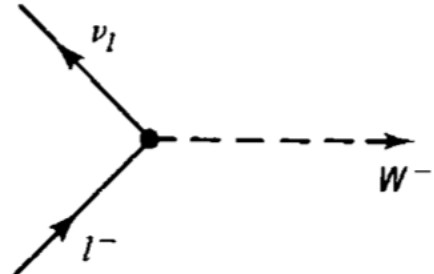
(a) The electromagnetic force



(b) The strong force



(c) The neutral weak force



(d) The charged weak force

Figure 1.2: Fundamental particle interactions of the three fundamental forces described by the Standard Model [2].

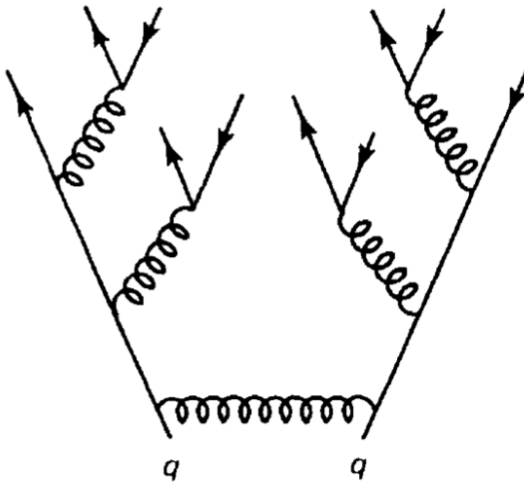


Figure 1.3: An example Feynmann diagram of jet production

¹⁸⁰ 1.2 QCD and Jets

¹⁸¹ While there is only one type of electric charge, there are three types of color charge; red, green,
¹⁸² and blue. In the process $q \rightarrow q + g$, the color of the quark can change. In order to conserve color
¹⁸³ charge, gluons are bicolored, and always carry some positive color charge and some negative color
¹⁸⁴ charge.

¹⁸⁵ Color charged particles can only exist in bound states which result in a neutral total color
¹⁸⁶ charge, a principle known as confinement. This requires that quarks and gluons exist in group
¹⁸⁷ states known as hadrons; either mesons in the case of two quarks or baryons in the case of three
¹⁸⁸ quarks. When a quark is separated from a hadron, confinement dictates that other colored objects
¹⁸⁹ are produced around the quark to obey confinement. An example of this process is shown in
¹⁹⁰ Figure 1.3. This ensemble of objects, generally a mixture of quarks and gluons, is termed a *jet*.
¹⁹¹ Jets are among the most common phenomenon observed by detectors at hadron colliders, and their
¹⁹² complex structure makes them a key focus of many physics analyses.

193 **1.3 Symmetries**

194 The Standard Model is a renormalizable quantum field theory that obeys the local symmetry

195 G_{SM} :

$$G_{SM} = SU(3)_C \times SU(2)_L \times U(1)_Y. \quad (1.1)$$

196 The $SU(3)_C$ symmetry component represents the non-Abelian gauge group of QCD. There
197 are 8 generators for the $SU_C(3)$ group which correspond to 8 types of gluon, each representing a
198 different superposition of color charge [3]. The $SU(2)_L \times U(1)_Y$ symmetry group represents the
199 electroweak sector of the Standard Model, which can be spontaneously broken into the electromag-
200 netic and weak sectors. There are 4 generators for this group, which correspond to four massless
201 gauge bosons W^1 , W^2 , W^3 , and B . From these massless gauge bosons are formed the massive
202 mediators of the weak force, the W^- , W^+ and Z^0 bosons, and the massless electromagnetic force
203 carrier, the photon γ . Spontaneous symmetry breaking and the process by which gauge bosons
204 acquire mass will be addressed in section 1.3.1.

205 Noether's theorem [4] stipulates that any continuous symmetry is associated with a conserved
206 quantity. In the Standard Model, this means that the $SU(3)_C$ symmetry gives rise to conservation of
207 color charge. The $SU(2)_L \times U(1)_Y$ symmetry gives rise to conservation of electromagnetic charge.
208 Conservation of spin results from the Poincaré symmetry described by the theory of special rela-
209 tivity, which combined with Noether's theorem gives us the conversation of energy, momentum,
210 and angular momentum.

211 The SM Lagrangian is invariant under CPT symmetry, or charge, parity, and time reversal.
212 Charge conjugation (C) transform a particle into it's corresponding antiparticle by reversing the
213 charge and other quantum numbers. Parity conjugation (P) reverses spatial coordinates, which
214 transforms left-handed particles into right-handed particles and vice-versa. Time reversal (T) is
215 the theoretical process of reversing time. The L subscript in the $SU(2)_L$ group indicates that this
216 symmetry only applies to left-handed fermions. As a result, the $W^{1,2,3}$ gauge bosons of $SU(2)_L$

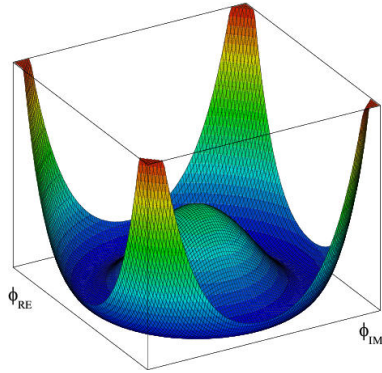


Figure 1.4: An illustration of the “hat shaped” potential of the Higgs field, resulting in a non-zero vacuum expectation value.

only interact with left handed particles, a process which maximally violates P-symmetry in the weak force. A small amount of the CP symmetry violation is also observed in the Standard Model, through the decays of strange flavored mesons [5]. The CPT theorem posits that the violation of CP symmetry implies that T-symmetry must also be violated, so that CPT is a preserved symmetry.

1.3.1 Spontaneous Symmetry Breaking and The Higgs Mechanism

Spontaneous symmetry breaking is the process by which a Lagrangian obeys a symmetry at high energies, but exhibits asymmetric behavior at lower energies. The electroweak symmetry group is spontaneously broken as $SU(2)_L \times U(1)_Y \rightarrow U(1)_{EM}$. The quantity conserved by the $SU(2)_L$ symmetry is weak isospin $T_{1,2,3}$, while the quantity conserved by $U(1)_Y$ symmetry is weak hypercharge Y . Below very high energies, the presence of the Higgs field causes the electroweak symmetry to break. The Higgs field is scalar field which forms a complex doublet of the $SU(2)$ symmetry group, with four degrees of freedom. The shape of the Higgs field potential, shown in Figure 1.4, results in a ground state with a non-zero vacuum expectation value; thus the Higgs field takes a non-zero value throughout all space, which breaks the symmetry of the weak isospin $SU(2)$ group.

The interaction with the Higgs field mixes the four massless gauge bosons $W^{1,2,3}$ and B . Three Higgs field degrees of freedom mix with the massless gauge bosons, resulting in three massive gauge bosons W^- , W^+ and Z^0 . The massless photon γ is created from the components of the

235 massless gauge bosons which do not interact with the Higgs field. The scalar Higgs boson arises
236 from the one unmixed degree of freedom the Higgs field. Spontaneous symmetry breaking also
237 violates the conservation of weak isospin and weak hypercharge, leaving only electromagnetic
238 charge ($Q = T_3 + \frac{1}{2}Y$) as a conserved quantity associated with the $U(1)_{EM}$ symmetry.

239 **1.4 Experimental Validation of the Standard Model**

240 The theoretical framework of the Standard Model coalesced into a unified theory in the mid-
241 20th century. A cascade of discoveries providing empirical evidence for the model followed
242 closely. In the 1960s, three quarks (up, down and strange) and four leptons (electron, muon,
243 and their associated neutrinos) were the known particulate building blocks of matter and the Stan-
244 dard Model. The discovery of the charm quark in 1974, through the observation of the J/ψ meson
245 [6][7], confirmed the existence of a fourth quark flavor. The discovery of the τ in 1975 [8] provided
246 the first evidence of a 3rd generation of matter. This was quickly followed by the observation of
247 the Υ meson in 1977 [9], which provided evidence for the existence of a fifth quark, the b quark
248 (bottom, or beauty). The existence of a 3rd generation of fermion also explained the observation
249 of CP violation in the weak force, as it allowed for the addition of a complex phase in the CKM
250 matrix (a unitary matrix which describes flavor mixing in the weak interaction). The top quark
251 (t) and tau neutrino (ν_τ) were predicted at this point as the final building blocks of three complete
252 generations of fermions, and they were discovered by experimental observation around the turn of
253 the 21st century [10] [11] [12].

254 The W and Z bosons were predicted by the Standard Model, but to observe them required the
255 construction of a particle accelerator powerful enough to produce them. They were finally observed
256 at CERN in 1983 by the UA1 and UA2 experiments [13] [14] at the newly constructed Super Proton
257 Synchrotron (SPS). Their masses were observed to be compatible with the masses predicted by the
258 Standard Model nearly a decade earlier. The final missing piece then was confirming the existence
259 of the Higgs, which again required the construction of a newer and more powerful collider. CERN
260 achieved this with the construction of the Large Hadron Collider (LHC), and in 2012 the ATLAS

261 and CMS experiments announced the discovery of the Higgs particle [15] [16].

262 **1.5 Limitations of the Standard Model**

263 While the Standard Model has enjoyed decades of experimental results which confirm its pre-
264 dictions, there are several glaring shortcomings. The observed phenomenon for which the Standard
265 Model provides no explanation are summarized below.

- 266 • Gravity - the Standard Model does not account for the fourth fundamental force of gravity.
- 267 • Dark Matter - there is no viable candidate to explain the existence of dark matter, a non-
268 interacting form of matter which must exist to account for gravitational observations which
269 cannot be explained by general relativity, such as the motion of galaxies, gravitational lens-
270 ing, and the structure of the universe [17].
- 271 • Matter-Antimatter asymmetry - the level of CP violation in the Standard Model isn't suf-
272 ficient to explain the large discrepancy between the amount of matter and the amount of
273 antimatter in the universe today, and the origins of this imbalance are not understood.
- 274 • Neutrino masses - the Standard Model assumes that neutrinos are massless and provides
275 no mechanism for them to acquire mass. However, observations of neutrino oscillations
276 indicates they posses some small non-zero mass [18].

277 In addition to these unexplained natural phenomenon, there are several questions about the
278 *naturalness* of the Standard Model. The principle of naturalness states that dimensionless ratios
279 between physical constants should be of order 1, and that nature should not be arbitrarily fine-
280 tuned. While this is largely an aesthetic argument, it points to many aspects of the Standard Model
281 for which there exists no natural explanation.

- 282 • Strong CP - while CP symmetry is violated in the weak force, observations indicate that it
283 is preserved by the strong force [19]. The Standard Model predicts that CP violation in the

284 strong force is possible. There is no principle which motivates this incongruity between the
285 weak force and strong force.

- 286 • Hierarchy Problem - The wide range of masses for elementary particles and the wide range of
287 scales at which the four fundamental forces operate is not motivated by the SM. Specifically,
288 it is not understood why the Higgs mass is observed to be well below the Plank scale λ ,
289 which is the energy level at which the effects of quantum gravity become significant. QFT
290 indicates that the Higgs mass is determined by contributions from all energy scales including
291 λ , meaning that its observed mass is inexplicably small.

292 The limitations of the Standard Model provide a road map for theoretical and experimental
293 particle physicists, who seek to develop new theories which account for these observations, and
294 then to find evidence which might support these *Beyond the Standard Model* (BSM) theories. The
295 next chapter will introduce the BSM theories which motivate the physics search presented in this
296 thesis.

Chapter 2: Physics Beyond the Standard Model

299 In light of the various phenomenon unexplained by the Standard Model, physicists have pro-
 300 posed various extensions to the Standard Model, collectively termed *Beyond the Standard Model*
 301 (BSM) theories. A particular focus of the physic programs at the Large Hadron Collider (LHC) are
 302 BSM models which suggest dark matter candidate particles. If these particles couple to Standard
 303 Model, they could be produced and observed at the LHC.

304 **2.1 Hidden Valley Models**

305 Hidden Valley (HV) models are a category of BSM models that allow for dark matter (DM)
 306 production at the LHC. They extend the Standard Model with an additional non-Abelian gauge
 307 group [20]. This introduces the possibility of a complex dark sector, which mirrors the complexities
 308 of Standard Model QCD, and introduces the possibility of dark quarks and gluons. The term
 309 “hidden valley” refers to the idea that the DM is hidden from the SM by a high-energy barrier, as
 310 illustrated in Figure ???. The dark sector is assumed to communicate with the Standard Model via
 311 a “portal”, or “messenger particle”, that can interact with both Standard Model and HV forces. For
 312 the s-channel scenario, the portal is considered to be a new massive mediator particle Z' .

313 The portal particle allows for the production of dark sector particles at hadron colliders. If
 314 dark quarks are produced via the decay $Z' \rightarrow q_D q_D$ they can hadronize and form dark jets. The
 315 properties of the dark jets are determined by the dynamics of the dark sector, which are explored in
 316 the subsequent section. Depending on the details of the model, the jets formed by the dark hadrons
 317 can be categorized as fully dark, semi-visible, leptonic, emerging, or other [20].

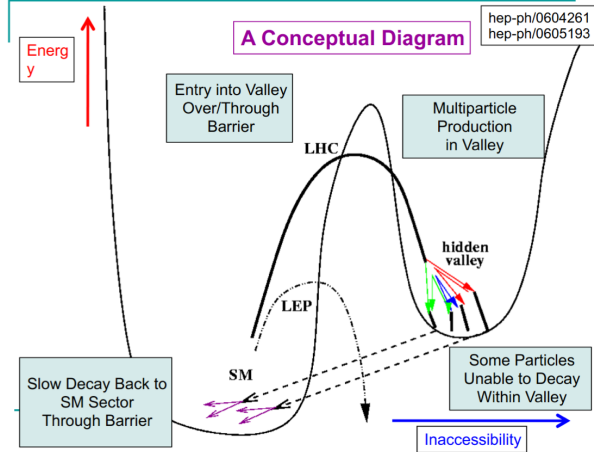


Figure 2.1: Illustration of the hidden valley potential

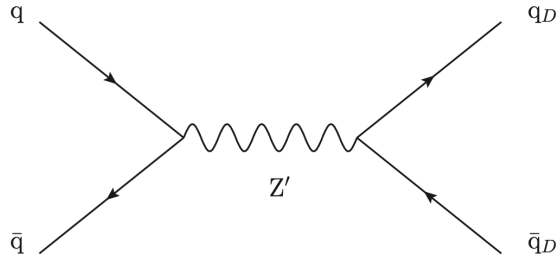


Figure 2.2: The massive mediator particle Z' of the s-channel realization of a HV model

318 2.2 Dark QCD

319 The theoretical underpinning of the semi-visible jet phenomenology is a dark sector with a
 320 gauge group $SU(N_d)$ leading to confinement at a scale Λ_d . For illustration, let's consider the
 321 case of an $SU(2)_d$ gauge theory, which gives rise to two dark fermionic generations $\chi_a = \chi_1, \chi_2$.
 322 Following the work of Timothy Cohen, et.al. we can write the fundamental dark Lagrangian as:

$$\mathcal{L}_{dark} \supset -\frac{1}{2} \text{Tr } G_{\mu\nu}^d G^{d\mu\nu} - \bar{\chi}_a (i \not{D} - M_{d,a}) \chi_a \quad (2.1)$$

323 The first term allows for the dark gluons to self-interact, while the second term enables the dark
 324 quarks to hadronize and acquire mass. The dark quarks are assumed to have a common mass M_d .
 325 The coupling strength of the strongly interacting dark quarks is termed α_d . At the confinement

326 scale Λ_d , the dark quarks can form bound states. At the scale $M_d \approx \Lambda_d$ a QCD-like show occurs.

327 The properties of the hadrons formed by the dark quarks are of particular importance to the
328 observed dark QCD dynamics. Dark-isospin number $U(1)_{1-2}$ and dark-baryon number $U(1)_{1+2}$
329 are accidental symmetries of the theory which determine the stability of the hadrons. In the case
330 of two dark flavors, six dark hadrons can be formed: four mesons ($\chi_1\bar{\chi}_1$, $\chi_2\bar{\chi}_2$, $\chi_1\bar{\chi}_2$, $\bar{\chi}_1\chi_2$) and
331 two baryons ($\bar{\chi}_1\bar{\chi}_2$, $\bar{\chi}_1\bar{\chi}_2$). The mesons $\chi_1\bar{\chi}_2$ and $\bar{\chi}_1\chi_2$ are charged under dark-isospin and will be
332 stable if this symmetry is unbroken. The baryons would also be stable as they are charged under
333 the dark-baryon number. These four stable hadrons become dark matter candidates of the theory.
334 The $\chi_1\bar{\chi}_1$ and $\chi_2\bar{\chi}_2$ mesons are not charged under either symmetry and are thus expected to decay.
335 The unstable mesons can decay into stable dark mesons, or into an off-shell Z' . The off-shell Z'
336 will then decay into two DM quarks or two SM quarks, and its products will continue to shower
337 until the final state particles are stable.

338 The number of stable and unstable dark states varies substantially depending on the details
339 of the model. The model discussed above can be generalized from $SU(2)_d$ to $SU(N)_d$, with any
340 number of colors N_c or flavors N_f . This affects the ratio of possible stable to unstable mesons,
341 which can directly impact the amount of missing energy. The fraction of missing energy is a
342 variable in many dark QCD models, and is especially important in the case of semi-visible jets.

343 2.3 Semi-visible Jets

344 A “semi-visible jet” occurs when the heavy Z' messenger particle decays into dark quarks,
345 which then hadronize in a QCD-like shower. If some of the dark hadrons are stable while others
346 decay to SM quarks via the off-shell Z' , a collimated mixture of visible and dark matter is formed
347 – this is termed a semi-visible jet. If the Z' messenger particle is produced at rest, the two jets will
348 be back-to-back in the transverse plane. If there is an imbalance in the amount of invisible particles
349 between the two jets, one of the jets will be observed to be aligned with missing transverse energy.

350 While there are a myriad of HV and dark QCD models, a handful of model parameters are most
351 important in determining the observable of these showers within a particle detector. The coupling

352 strength α_d is one of the most important, as it controls the fraction of dark hadrons emitted in the
353 shower and their average p_T . The mass of the dark quarks directly impacts the jet mass. If the
354 masses of the dark quark flavors are comparable, the ratio of stable to unstable dark hadrons will
355 be approximately 1:1. However, if there is a mass splitting, stable or unstable dark hadrons may
356 be favored, which impacts the amount of missing energy observed.

357 The ratio of stable to unstable dark hadrons in the shower is a critical variable for capturing the
358 behavior of dark showers. This value is termed r_{inv} :

$$r_{inv} = \frac{\# \text{ of stable hadrons}}{\# \text{ of hadrons}} \quad (2.2)$$

359 Events containing jets aligned with missing transverse momentum are generally considered to
360 be misreconstructed by other DM searches, and therefore discarded. This class of final states is
361 therefore largely uncovered by existing DM searches. The nature of the dark hadron shower is
362 determined by the following parameters: the Z' mass $m_{Z'}$, the Z' couplings to visible and dark
363 quarks g_q and g_{q_D} , the number of dark colors and flavors, the characteristic scale of the dark sector
364 confinement Λ_D , the scale of the dark hadrons m_D , and the average fraction of stable hadrons in
365 the decay r_{inv} . The coupling to SM quarks determines the Z' production cross section.

Chapter 3: The Large Hadron Collider

368 The Large Hadron Collider (LHC) is a 26.7 km circular high-energy particle accelerator, span-
 369 ning the Swiss-French border near the city of Geneva, Switzerland [21]. The LHC occupies the
 370 tunnel constructed in 1989 for the Large Electron-Positron (LEP) Collider, and reaches a maxi-
 371 mum depth of 170m below the surface. The LHC is operated by the European Organization for
 372 Nuclear Research (CERN), the largest international scientific collaboration in the world.

373 The LHC accelerates protons and heavy ions, and collides them at four interaction points
 374 around the ring, with a design center-of-mass energy per collision of $\sqrt{s} = 14$ TeV. Each interaction
 375 point is home to one of four detector experiments, which study the products of the collisions. The
 376 largest of these experiments is the ATLAS detector, a general purpose detector designed to study
 377 the Standard Model and search for new physics that could be produced in LHC collisions [22].
 378 The CMS detector is another general purpose detector, designed and operated independently of the
 379 ATLAS detector, but intended to probe the same range of physics [23]. The ALICE experiment is
 380 a dedicated heavy ion experiment, and the LHC-b experiment is a dedicated *b*-physics experiment
 381 [24] [25].

382 This chapter will cover the multi-component accelerator complex powering the LHC, the state-
 383 of-the-art magnets which steer the particle beams, measurements of the intensity and number of
 384 collisions produced by the LHC, and finally an overview of LHC activities in the past, present, and
 385 future.

³⁸⁶ **3.1 Accelerator Physics**

³⁸⁷ **3.1.1 The Journey of a Proton**

³⁸⁸ From 2010 - 2018, the protons which fed the LHC started as hydrogen gas. The electrons were
³⁸⁹ removed from the hydrogen atoms through the use of strong electric fields. The linear accelerator
³⁹⁰ LINAC2 then accelerated the protons to an energy of 50 MeV. Between 2018 and 2020, LINAC2
³⁹¹ was replaced with LINAC4, which instead accelerates H^- ions, hydrogen atoms with two electrons.
³⁹² LINAC4 is capable of accelerating the H^- ions to 160 MeV. Before injection to the next part of
³⁹³ the acceleration chain, both electrons are stripped from the H^- ions, leaving just protons. From
³⁹⁴ here the protons enter the Proton Synchrotron booster, where they are accelerated up to 1.4 GeV of
³⁹⁵ energy. Subsequently they are sorted into bunches separated in time by 25 ns, where each bunch
³⁹⁶ contains approximately 10^{11} protons. Next the bunches pass through the Proton Synchrotron (PS)
³⁹⁷ and the Super Proton Synchrotron (SPS), where they reach energies of 25 GeV and 450 GeV
³⁹⁸ respectively. Finally they are injected into the LHC as two beams traveling in opposite direction.
³⁹⁹ The original design allowed each beam to be accelerated up to 7 TeV of energy. Due to limitations
⁴⁰⁰ in the performance of the superconducting LHC magnets, the highest energy actually achieved by
⁴⁰¹ the LHC beams during Run 2 was 6.5 TeV, giving a collision center-of-mass energy of $\sqrt{s} = 13$
⁴⁰² TeV [26]. Figure 3.1 shows the full LHC accelerator complex.

⁴⁰³ Acceleration in the LHC is performed by eight radio frequency (RF) cavities located around the
⁴⁰⁴ ring. Each RF cavity produces a 2 MV electric field oscillating at 40 MHz. The 40MHz oscillation
⁴⁰⁵ produces a point of stable equilibrium every 2.5 ns. These points of equilibrium are synchronized
⁴⁰⁶ with the occurrence of the proton bunches produced in the PS – a proton bunch occupies one out
⁴⁰⁷ of every ten points of stable equilibrium, such that the bunches maintain a 25 ns spacing [26].

⁴⁰⁸

The CERN accelerator complex Complexe des accélérateurs du CERN

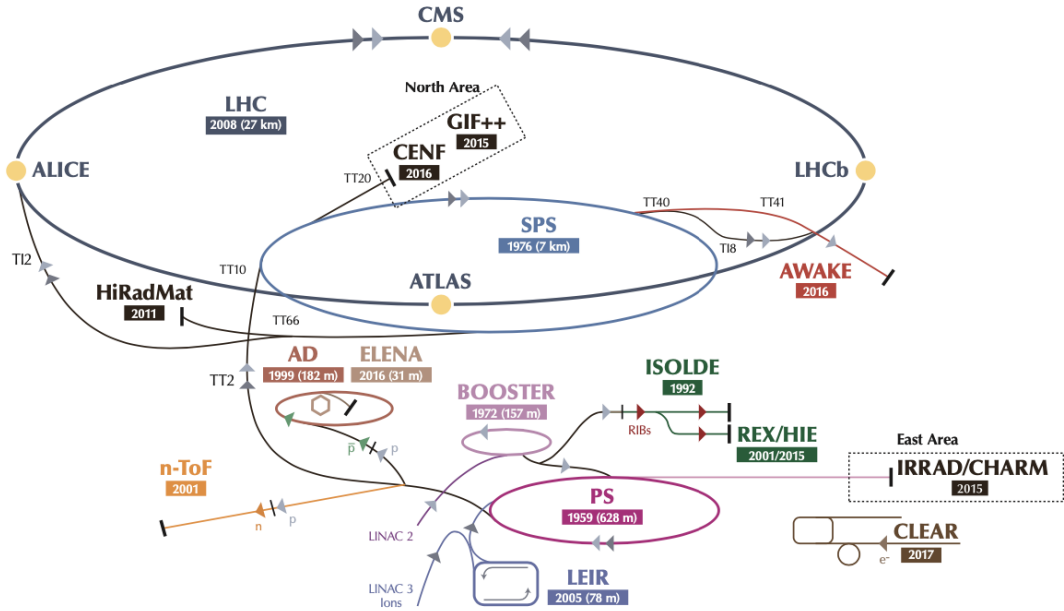


Figure 3.1: The LHC accelerator complex at CERN [27]

409 3.1.2 Magnets

410 In addition to the acceleration cavities, the LHC houses 9593 superconducting magnets which
 411 direct and focus the proton beam on its 27 kilometer journey. The magnets are comprised of super-
 412 conducting Niobium-Titanium coils cooled to 1.9K by superfluid helium. As the beams approach
 413 one of the four collision points around the ring, multipole magnets focus and squeeze the beam for
 414 optimal collisions [26].

415 The LHC is divided into sections, where each section contains an arc and a straight insertion. The arcs are composed of 1232 large dipole magnets which bend the beam
 416 to follow the roughly circular 27 km path. The main dipoles generate powerful 8.3 tesla magnetic
 417 fields to achieve this bend. Each dipole magnet is 15 meters long and weighs 35 tonnes. The
 418 dipoles work in conjunction with quadrupole magnets, which keep the particles in a focused beam,
 419 and smaller sextupole, octupole and decapole magnets which tune the magnetic field at the ends of
 420 the dipole magnets [28].

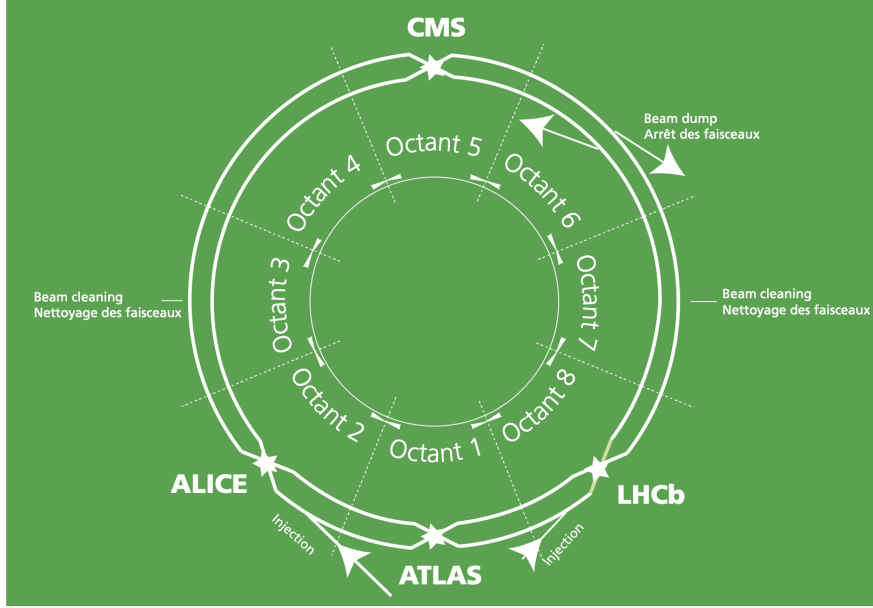


Figure 3.2: The octants of the LHC and location of various beam activities [26]. Stars indicate the locations of beam collisions, and the associated detectors recording the outcome of those collisions.

422 The straight insertion sections have different purposes depending on their location around the
 423 ring: beam collisions, beam injection, beam dumping, or beam cleaning. At the four collision
 424 points, insertion magnets squeeze the beam to ensure a highly focused collision. This is accom-
 425 plished with a triplet of quadrupole magnets, which tighten the beam from 0.2 millimeters to just
 426 16 micrometers in diameter. Insertion magnets also clean the beam, which prevents stray particles
 427 from hitting sensitive components throughout the LHC. When the LHC is ready to dispose of a
 428 beam of particles, beam dump magnets deflect the path of the beam into a straight line towards
 429 a block of concrete and graphite that stops the beam. A dilution magnet then reduces the beam
 430 intensity by a factor of 100,000 before the final stop [28]. Figure 3.2 shows the locations various
 431 beam activities.

432 3.2 Luminosity

433 Collisions at the LHC occur when the two beams of proton bunches cross at one of the four
 434 interaction points. The intensity of collisions is described by the instantaneous luminosity, the

435 formula for which is given in equation 3.1.

$$L = \frac{fN_1N_2}{4\pi\sigma_x\sigma_y} \quad (3.1)$$

436 Here f is the revolution frequency, N_1 and N_2 are the number of particle per bunch for each
437 beam, and σ_x , σ_y are the horizontal and vertical beam widths.

438 The instantaneous luminosity gives the number of the collisions that could be produced at the
439 interaction point per unit of cross-sectional area per unit of time, generally expressed in $\text{cm}^{-2}\text{s}^{-1}$.
440 The integrated luminosity is obtained by integrating the instantaneous luminosity over a given
441 block of time, and measures the total number of collisions which have occurred during that op-
442 eration period. The total integrated luminosity is directly correlated with the size of the datasets
443 collected by the LHC experiments. Total integrated luminosity for Run 2 is illustrated in Figure
444 3.3.

445 High levels of instantaneous luminosity result in multiple pp collisions per bunch crossing,
446 which leads to an effect known as *pileup*. Pileup poses a challenge for detector physics, as recon-
447 structing the products of multiple simultaneous events is far more challenging than reconstructing
448 a single event with no pileup. Pileup conditions vary from year-to-year and run-to-run of LHC op-
449 eration, and the impact of these conditions are taken into account when analyzing the data, as will
450 be discussed further in Chapter 5. Measurement of pileup conditions during Run 2 are illustrated
451 in Figure 3.3.

452 The design peak luminosity of the LHC is $1.0 \times 10^{34} \text{ cm}^{-2}\text{s}^{-1}$. During Run 1 of the LHC the
453 peak instantaneous luminosity was $0.8 \times 10^{34} \text{ cm}^{-2}\text{s}^{-1}$. Over the course of Run 1 the LHC collected
454 a total integrated luminosity of 5.46 fb^{-1} at $\sqrt{s} = 7 \text{ TeV}$, and 22.8 fb^{-1} at $\sqrt{s} = 8 \text{ TeV}$. Following the
455 first long shutdown and upgrade phase of operations, the LHC achieved a center of mass energy
456 $\sqrt{s} = 13 \text{ TeV}$ at the beginning of Run 2 in 2015. The LHC was also able to deliver 2.0×10^{34}
457 $\text{cm}^{-2}\text{s}^{-1}$ peak instantaneous luminosity, double the design value. During LHC Run 2, from 2015-
458 2018, the LHC delivered 156 fb^{-1} of integrated luminosity for proton-proton collisions. Run 3 of

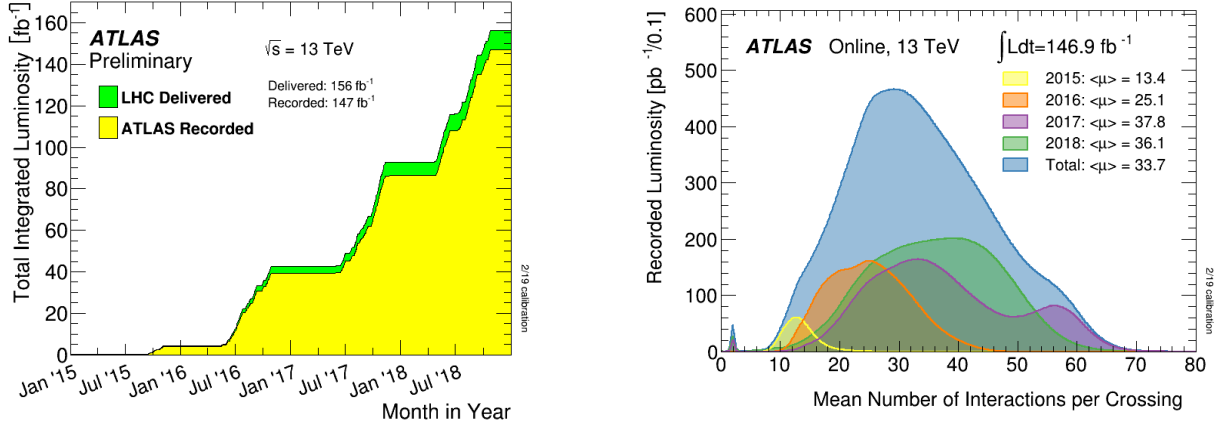


Figure 3.3: (Left) Total integrated luminosity over the course of Run 2. (Right) Average number of pp interactions per bunch crossing in Run 2. Each curve is weighted by the integrated luminosity for the year.

459 the LHC began in 2022, and is expected to deliver 250 fb^{-1} of integrated luminosity to the ATLAS
 460 and CMS experiments by 2026 [29].

461 The goal of LHC physic analyses is to find and study rare events produced by interesting
 462 physics processes. The cross section σ of a given process indicates the probability of that process
 463 occurring given the beam conditions of the LHC. Multiplying the cross section by the integrated
 464 luminosity of a dataset gives the expected number of events for that process within the dataset.

$$N_{\text{events}} = \int \sigma L(t) dt = \mathcal{L} \times \sigma \quad (3.2)$$

465 The cross section for most processes of interest, especially BSM processes, is several orders of
 466 magnitude below the total cross section for the LHC. Therefore maximizing the number of events
 467 produced in collisions is crucial to increase the likelihood of producing events from processes of
 468 interest. For this reason, maximizing instantaneous luminosity is a key factor in accelerator design
 469 and operation, while mitigating the resulting pileup effects is a key component in detector design
 470 and operation.

471 **3.3 LHC Timeline**

472 The first proton-proton collisions at the LHC were achieved in 2010 with a center-of-mass
473 energy of $\sqrt{s} = 7$ TeV. Run 1 of the LHC took place between 2010 and early 2013, during which
474 time the center-of-mass collision energy increased from 7 TeV to 8 TeV. Figure 3.4 shows an
475 overview of LHC activities beginning in 2011, in the midst of Run 1. The data collected during
476 Run 1 led to the discovery of the Higgs Boston in 2012 [30].

477 Between 2013 and 2015 the LHC underwent the first Long Shutdown (LS1) during which
478 time maintenance and renovation was performed on the accelerator chain, including the repair and
479 consolidation of the high-current splices which connect the super-conducting LHC magnets. Run
480 2 of the LHC took place from 2015 to 2018 and achieved a center-of-mass energy of $\sqrt{s} = 13$ TeV.
481 Analysis of data collected in Run 2 is still on going, and is the subject of study in this thesis.

482 Between 2018 and 2022 the LHC underwent the second Long Shutdown (LS2), allowing for
483 further detector and accelerator maintenance and upgrades. Key improvements to the LHC in-
484 cluded the improvement of the insulation for over 1200 diode magnets, and the upgrade from
485 LINAC2 to LINAC4 mentioned in Section 3.1.1. Run 3 of the LHC began in 2022 and achieved a
486 center-of-mass energy of $\sqrt{s} = 13.6$ TeV.

487 Run 3 is scheduled to continue through 2026, at which point the LHC machine and detectors
488 will undergo upgrades for the *high luminosity* LHC (HL-LHC). The HL-LHC will increase the
489 instantaneous machine luminosity by a factor of 5 - 7.5 with respect to the nominal LHC design.
490 The bottom panel of Figure 3.4 shows an overview of the preparation work for the HL-LHC that
491 has been going on concurrently with Run 1, 2, and 3 of the LHC [31].



Figure 3.4: Timeline of LHC and HL-LHC activities [29]. Integrated luminosity estimates are approximate, and not reflective of the exact amount delivered to each experiment.

492

493

Chapter 4: The ATLAS Detector

494 The ATLAS detector (**A Toroidal LHC ApparatuS**) is one of two general purpose physics
495 detectors designed to study the products of proton-proton collisions at the LHC. The detector is
496 composed of a variety of specialized subsystems, designed to fully capture a wide array of physics
497 processes. The apparatus is 25m high, 44m in length, and weighs over 7000 tons [32]. The LHC
498 beam pipes direct proton beams to an interaction point at the center of ATLAS, and the cylindrical
499 detector design captures a complete 360° view of the *event*, tracking all particles that result from
500 the collision.

501 The main components of the ATLAS detector are the Inner Detector (ID) which provides high
502 precision tracking of charged particles leaving the collision vertex, the calorimeter system which
503 measures the energy of electromagnetic and hadronic objects, and the Muon Spectrometer (MS)
504 which gives detailed information about muons that reach the outer radii of the detector. Two
505 magnet systems, a 2 T solenoid magnet surrounding the ID, and a 0.5-1.0 T toroid magnet system
506 situated throughout the MS, produce magnetic fields which bend the trajectory of charged particles
507 traversing the detector. In addition to the main detector components, dedicated forward detectors
508 monitor beam conditions and instantaneous luminosity, and an online trigger system reduces the
509 data rate to a manageable level for storage. Each of these components will be discussed in further
510 detail in this chapter.

511 **4.1 Coordinate System and Geometry**

512 The ATLAS detector employs a right hand cylindrical coordinate system. The z axis is aligned
513 with the beam line, and the x-y plane sits perpendicular to the beam line. The coordinate system
514 origin is centered on the detector, such that the origin corresponds with the interaction point of the

515 two colliding beams. The detector geometry is usually characterized by polar coordinates, where
516 the azimuthal angle ϕ spans the x-y plane. The polar angle θ represents the angle away from the
517 beam line, or z axis. $\theta = 0$ aligns with the positive z -axis, and $\phi = 0$ aligns with the positive x-axis.

518 The polar coordinate θ is generally replaced by the Lorentz invariant quantity *rapidity* or y :

$$y = \frac{1}{2} \ln\left(\frac{E + p_z}{E - p_z}\right). \quad (4.1)$$

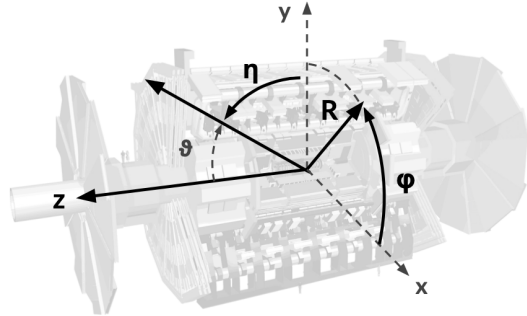
519 This substitution is advantageous because objects in the detector are traveling at highly rela-
520 tivistic speeds. The relativistic speed also means that the masses of the particles are generally small
521 compared to their total energy. In the limit of zero mass, the rapidity y reduces to the pseudorapid-
522 ity η , which can be calculated directly from the polar angle θ :

$$\eta = -\ln\left(\frac{\theta}{2}\right). \quad (4.2)$$

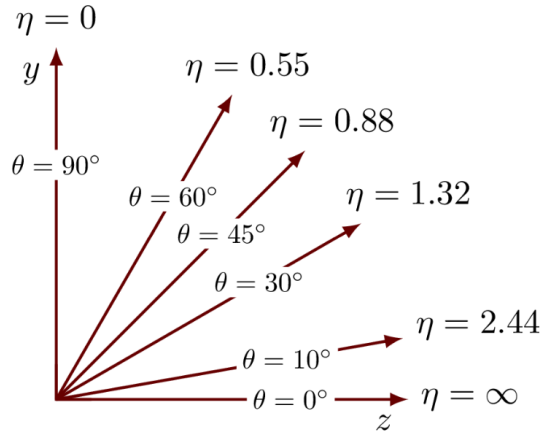
523 The distance between physics objects in the detector is generally expressed in terms of the solid
524 angle between them ΔR :

$$\Delta R = \sqrt{\Delta\phi^2 + \Delta\eta^2} \quad (4.3)$$

525 Figure 4.1a depicts the orientation of the coordinate system with respect to the ATLAS detector,
526 while Figure 4.1b illustrates the relationship between θ , η , and the beamline axis z . Direct or “head
527 on” proton-proton collisions are more likely to result in objects whose momentum is directed
528 along transverse plane (low $|\eta|$); glancing proton-proton collisions are more likely to result in
529 objects whose momentum is directed along the z -axis (high $|\eta|$). Due to the difference in the
530 nature of these collisions, as well as the cylindrical design of the ATLAS detector, the detector
531 is divided into regions of low and high η . Each subsystem has a “central” or “barrel” region
532 covering low $|\eta|$, while the “forward” or “end-cap” regions cover the area up to $|\eta| = 4.9$. Each of
533 the three main ATLAS subsystems will be discussed in the following sections.



(a) The ATLAS geometry



(b) Relationship between η and θ

Figure 4.1: ATLAS coordinate system and geometry

534 4.2 Inner Detector

535 The Inner Detector (ID) is the ATLAS subsystem closest to the interaction point. The primary
 536 purpose of the ID is to determine the charge, momentum, and trajectory of charged particles pass-
 537 ing through the detector. With this information the ID is also able to precisely determine interaction
 538 vertices.

539 The ID is composed of three sub-detectors; the Pixel Detector, the Semiconductor Tracker
 540 (SCT) and the Transition Radiation Tracker (TRT). Figure 4.2 shows the location of these three
 541 subsystems with respect to each other and the interaction point.

542 4.2.1 Pixel Detector

543 The pixel detector is the first detector encountered by particles produced in LHC collisions.
 544 The original pixel detector consists of 3 barrel layers of silicon pixels, positioned at 5 cm, 9 cm
 545 and 12 cm from the beamline. There are also 3 disks on each end-cap positioned 50 - 65 cm from
 546 the interaction point, providing full coverage for $|\eta| < 2.2$. The layers are comprised of silicon
 547 pixels each measuring $50 \times 400 \mu\text{m}^2$, with 140 million pixels in total. The pixels are organized
 548 into modules, which each contain a set of radiation hard readout electronics chips. In 2014, the
 549 Insertable B-layer (IBL) was installed, creating a new innermost layer of the pixel detector sitting

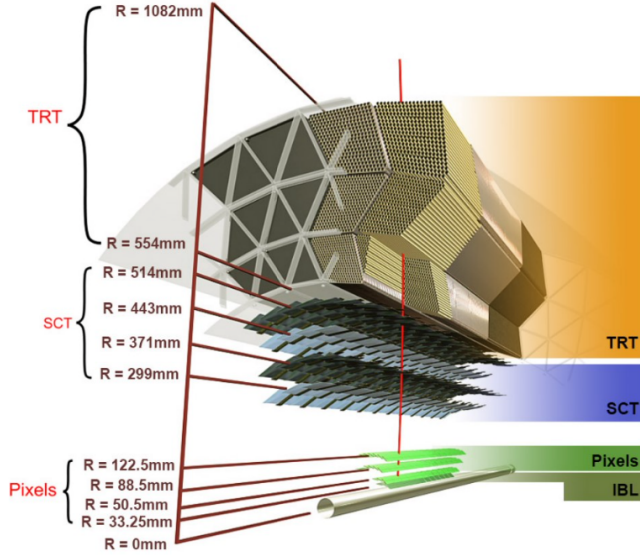


Figure 4.2: A 3D visualization of the structure of the ID in the barrel region [33]

550 just 3.3 cm from the beamline. The pixels of the IBL measure $50 \mu\text{m}$ by $250 \mu\text{m}$, and cover
 551 a pseudo-rapidity range up to $|\eta| < 3$. The IBL upgrade enhances the pixel detector's ability
 552 to reconstruct secondary vertices associated with short-lived particles such as the b-quark. The
 553 improved vertex identification also helped compensate for increasing pile-up in Run 2 [32].

554 4.2.2 Semiconductor Tracker

555 The SCT provides at least 4 additional measurements of each charged particle. It employs the
 556 same silicon technology as the Pixel Detector, but utilizes larger silicon strips which measure $80 \mu\text{m}$
 557 by 12.4 cm . The SCT is composed of 4 barrel layers, located between 30 cm and 52 cm from
 558 the beamline, and 9 end-cap layers on each side. The SCT can distinguish tracks that are separated
 559 by at least $200 \mu\text{m}$.

560 4.2.3 Transition Radiation Tracker

561 The TRT provides an additional 36 hits per particle track. The detector relies on gas filled
 562 straw tubes, a technology which is intrinsically radiation hard. The straws which are each 4 mm in
 563 diameter and up to 150 cm in length and filled with xenon gas. The detector is composed of about

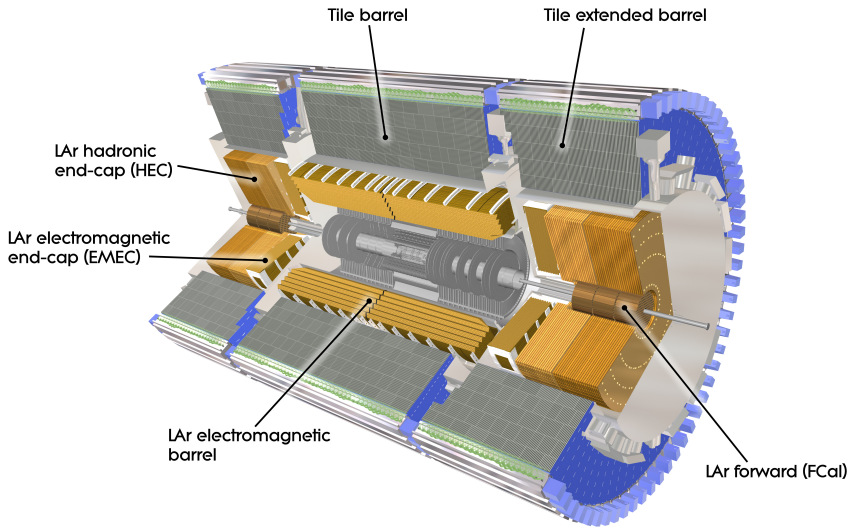


Figure 4.3: ATLAS calorimetry system [34]

564 50000 barrel region straws and 640000 end-cap straws, comprising 420000 electronic readout
 565 channels. Each channel provides a drift time measurement with a spatial resolution of $170\text{ }\mu\text{m}$ per
 566 straw. As charged particles pass through the many layers of the detector, transition radiation is
 567 emitted. The use of two different drift time thresholds allows the detector to distinguish between
 568 tracking hits and transition radiation hits.

569 4.3 Calorimeters

570 The ATLAS calorimeter system is responsible for measuring the energy of electromagnetically
 571 interacting and hadronically interacting particles passing through the detector. The calorimeters are
 572 located just outside the central solenoid magnet, which encloses the inner detectors. The calorime-
 573 ters also stop most known particles, which the exception of muons and neutrinos, preventing them
 574 from traveling to the outermost layers of the detector. The ATLAS calorimetry system is composed
 575 of two subsystems - the Liquid Argon (LAr) calorimeter for electromagnetic calorimetry and the
 576 Tile calorimeter for hadronic calorimetry. The full calorimetry system is shown in Figure 4.3.

577 4.3.1 Liquid Argon Calorimeter

578 The LAr calorimeter is a sampling calorimeter designed to trigger on and measure the ener-
579 gies of electromagnetic (EM) particles, as well as hadronic particles in the high η regions. It is
580 divided in several regions, as shown in Figure 4.3. For the region $|\eta| < 1.4$, the electromagnetic
581 barrel (EMB) is responsible for EM calorimetry, and provides high resolution energy, timing,
582 and position measurements for electrons and photons passing through the detector. The elec-
583 tromagnetic endcap (EMEC) provides additional EM calorimetry up to $|\eta| < 3.2$. In the re-
584 gion $1.4 < |\eta| < 3.2$, the hadronic endcap (HEC) provides hadronic calorimetry. For hadronic
585 calorimetry in the region $|\eta| < 1.4$, corresponding to a detector radii > 2.2 m, the less expensive
586 tile calorimeter (discussed in the next section) is used instead. A forward calorimeter (FCAL)
587 extends the hadronic calorimetry coverage up to $3.1 < |\eta| < 4.8$ [35].

588 The LAr calorimeter is composed of liquid argon sandwiched between layers of absorber mate-
589 rial and electrodes. Liquid argon is advantageous as a calorimeter active medium due to its natural
590 abundance and low cost, chemical stability, radiation tolerance, and linear response over a large
591 energy range [36]. The calorimeter is cooled to 87k by three cryostats: one barrel cryostat encom-
592 passing the EMB, and two endcap cryostats. The barrel cryostat also encloses the solenoid which
593 produces the 2T magnetic field for the inner detector. Front-end electronics are housed outside the
594 cryostats and are used to process, temporarily store, and transfer the calorimeter signals.

595 **Electromagnetic Calorimeter**

596 For the electromagnetic calorimeters, the layers of electrodes and absorber materials are ar-
597 ranged in an an accordion shape, as illustrated in Figure 4.4. The accordion shape ensures that
598 each half barrel is continuous in the azimuthal angle, which is a key feature for ensuring consistent
599 high resolution measurements. Liquid argon permeates the space between the lead absorber plates,
600 and a multilayer copper-polymide readout board runs through the center of the liquid argon filled
601 gap.

602 The detection principle for the LAr calorimeter is the current created by electrons which are

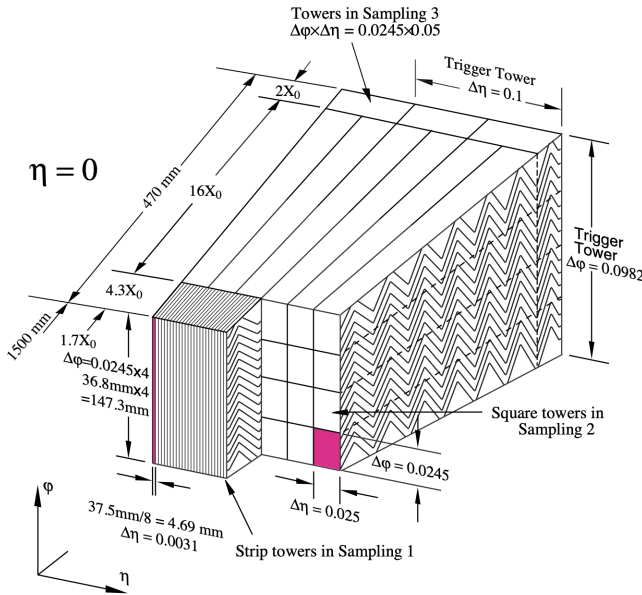


Figure 4.4: Diagram of a segment of the EMB, demonstrating the accordion plate arrangement [35]

603 released when a charged particle ionizes the liquid argon. In the barrel region, the electrons are
 604 driven towards the center electrodes by a 2000 V potential with a drift time of less than 450 ns [37].
 605 In the end-caps the voltage varies as a function of the radius in order to maintain a flat response
 606 [35]. The amount of current produced by the ionized electrons is proportional to the energy of
 607 the particle creating the signal. Figure 4.5 shows the shape of the signal produced in the LAr
 608 calorimeter, before and after it undergoes shaping during the readout process. The shaping of the
 609 pulse enforces a positive peak and a negative tail, which ensures that subsequence pulses can be
 610 separated with the precision required for the 25 ns LHC bunch spacing [35].

611 Hadronic End-cap Calorimeter

612 The HEC sits radially beyond the EMEC. The copper absorber plates in the HEC are oriented
 613 perpendicular to the beamline, with LAr as the active medium. Each end-cap is divided into two
 614 independent wheels; the inner wheel uses 25 mm copper plates, while the outer wheel uses 50 mm
 615 plates as a cost saving measure. In each wheel, the 8.5 mm plate gap is crossed by three parallel

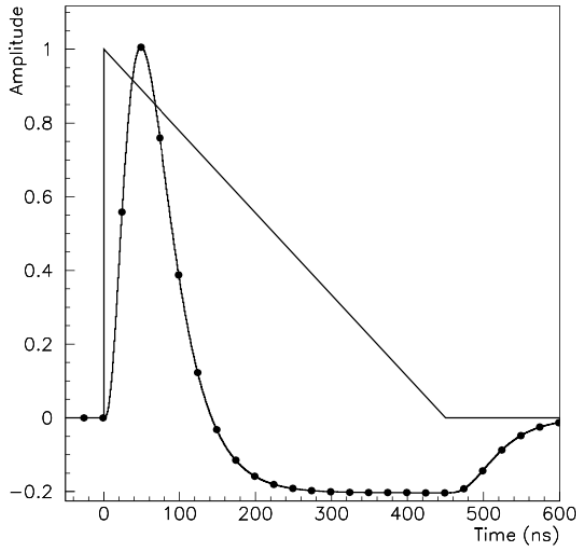


Figure 4.5: A LAr pulse as produced in the detector (triangle) and after shaping (curve) [35]

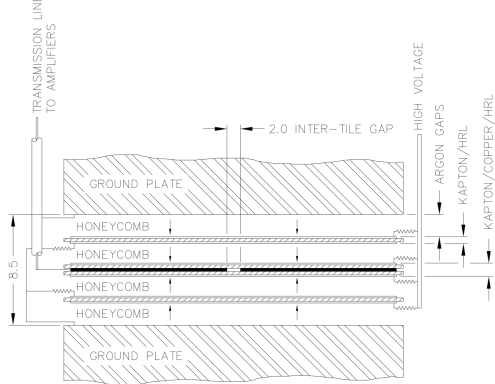


Figure 4.6: Readout gap structure in HEC [35]

616 electrodes, creating an effective drift distance of 1.8 mm. This gap is illustrated in Figure 4.6.
 617 Each wheel is divided into 32 wedge-shaped modules, each containing their own set of readout
 618 electronics.

619 **Forward Calorimeter**

620 The forward range is covered by the FCal, which provides both EM and hadronic calorimetry.
 621 It is composed of three active cylindrical modules; one EM module with copper absorber plates,
 622 and two hadronic modules with tungsten absorber plates. The plates are oriented perpendicular to

623 the beamline, and LAr is used as the active material throughout. The electrodes of the FCal consist
624 of tubes that run parallel to the beam line, arranged in a honeycomb pattern. The resulting LAr
625 gaps are as small as $250\ \mu\text{m}$, which enables the FCal to handle the large influx of particles in the
626 forward region [35].

627 4.3.2 Tile Calorimeter

628 The Tile Calorimeter (TileCal) provides hadronic calorimetry in the region $\eta < 1.7$, and sur-
629 rounds the LAr calorimeter. It is responsible for measurements of jet energy and jet substructure,
630 and also plays an important role in electron isolation and triggering (including muons) [38]. Tile-
631 Cal is composed of 3 sections, as shown in Figure 4.3; a barrel calorimeter sits directly outside the
632 LAr EMB and provides coverage up to $\eta < 1.0$. Two extended barrel sections sit outside the LAr
633 endcaps and cover the region $0.8 < \eta < 1.7$.

634 TileCal is a sampling calorimeter composed of steel and plastic scintillator plates as illustrated
635 in Figure 4.7. A total of 460,000 scintillators are read out by wavelength-shifting fibers. The
636 fibers are gathered to define cells and in turn read out by photomultiplier tubes, which amplify
637 the signal and convert it to an electrical signature. Each cell has an approximate granularity of
638 $\Delta\eta \times \Delta\phi = 0.1 \times 0.1$. Each barrel is divided azimuthally into 64 independent modules, an example
639 of which is show in Figure 4.7. The modules are each serviced by front-end electronic housed in a
640 water-cooled drawer on the exterior of the module.

641 The detection principle of the TileCal is the production of light from hadronic particles inter-
642 acting with the scintillating tiles. When a hadronic particle hits the steel plate, a shower of particles
643 are produced. The interaction of the shower with the plastic scintillator produces photons, the num-
644 ber and intensity of which are proportional to the original particle's energy.

645

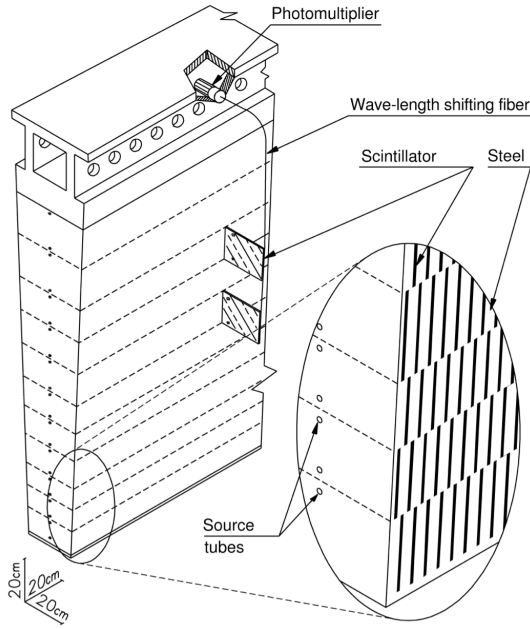


Figure 4.7: TileCal wedge module [38]

646 4.4 Muon Spectrometer

647 Unlike electrons, photons, and hadrons, muons interact minimally with the ATLAS calorimeters, and can pass through large amounts of detector material without stopping. The ATLAS Muon
 648 Spectrometer (MS) provides additional tracking information to improve the identification and measurement of muons. The MS comprises the outermost layers of the detector, and is interspersed
 649 with toroid magnets (discussed in Section 4.5), which provide a magnetic field of approximately
 650 0.5 T. The magnetic field bends the trajectory of the muons as they pass through the detector, and
 651 the degree of the bend is directly correlated with the muon momentum. The path of the muon is
 652 primarily measured by hits in three layers of Monitored Drift Tube (MDT) precision chambers,
 653 which cover the range $|\eta| < 2.7$. The barrel layout of the MS is show in Figure 4.8.

656 Muon triggering is provided by three layers of Resistive Plate Chambers (RPC) in the barrel
 657 ($|\eta| < 1.05$), and 3 - 4 layers of Thin Gap Chambers (TGC) in the end-caps ($1.05 < |\eta| < 2.4$).
 658 RPCs and TGCs also provide muon track measurements in the non-bending coordinate (ϕ). RPCs
 659 are constructed from two parallel resistive plates separated by a 2mm gap filled with a sensitive

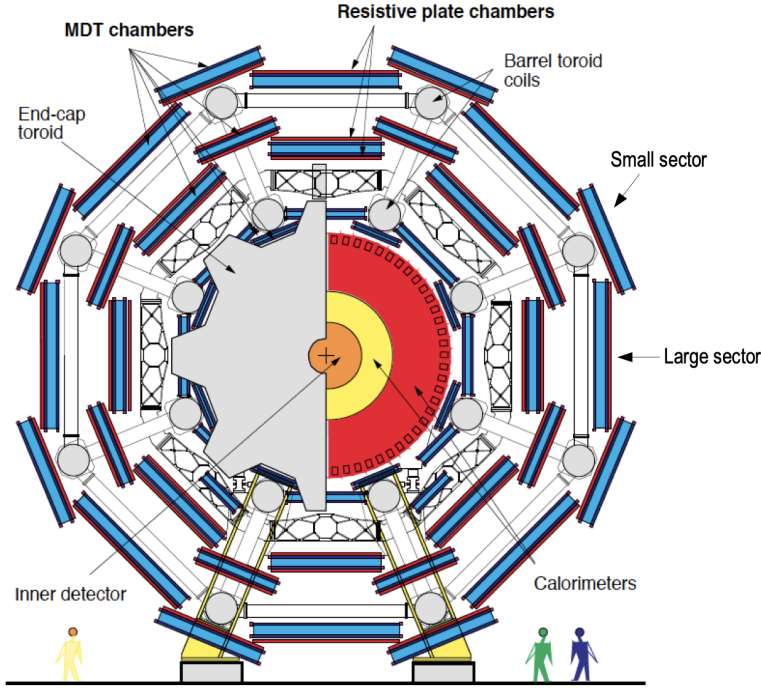


Figure 4.8: Cross section view of the muon spectrometer system [39]

660 gas mixture. This provides a total of six independent measurements for each muon track, with a
 661 spatial resolution of ~ 1 cm and a time resolution of ~ 1 ns. Time measurements from the RPCs
 662 are primarily associated to hits in the MDT precision chambers to determine the bunch crossing.
 663 The time measurement is also used to reject cosmic muons, and to search for delayed signals.
 664 TCGs provide triggering in the end-cap regions, and consist of parallel $30\ \mu\text{m}$ wires suspended
 665 in a sensitive gas mixture. TCGs provide high radiation tolerance and a fast response time, both
 666 features that are necessary for handling the high flux of muons in the forward region [39].

667 Precision measurements of muon momentum and position are primarily achieved by MDTs.
 668 The MDTs are constructed from 30 mm diameter tubes, permeated by a gas mixture of 93% Ar and
 669 7% CO₂. The average single-tube spatial resolution is $80\ \mu\text{m}$. Each chamber consists of six drift
 670 tube layers, which together provide a muon track segment resolution of $35\ \mu\text{m}$. The momentum
 671 of the muons can be calculated from the bend in the muon trajectory as they pass through the
 672 0.5T magnetic field provided by the toroids. For a $p_T = 1$ TeV track, the average p_T resolution is
 673 11%. In the inner most end-cap wheels, Cathode Strip Chambers (CSC) are used instead of MDTs,

674 covering the region $2.0 < |\eta| < 2.7$. CSCs are multi-wire proportional chambers, with a cathode
675 strip readout. The CSCs have a spatial resolution in the range of $50 \mu\text{m}$, and a maximum drift time
676 of about 30 ns, which makes them superior for handling the high flux of particles in the forward
677 region [40].

678 **4.5 Magnet System**

679 The ATLAS magnet system consists of four sets of superconducting magnets: a barrel solenoid,
680 a barrel toroid, and two end-cap toroids. The solenoid magnet produces a 2T magnetic field re-
681 sponsible for bending the trajectories of charged particles as they pass through the inner detector.
682 The three toroid magnets provide a field of 0.5 - 1 T and curve the path of muons passing through
683 the muon spectrometer.

684 The inner solenoid magnet is composed of over 9 km of niobium-titanium superconductor
685 wires, which are imbedded into strengthen pure aluminum strips. The solenoid is just 4.5 cm
686 thick, which minimizes interactions between the magnet material and particles passing through the
687 detector. It is housed in the LAr cryostat, as described in section 4.3.1, which further reduces the
688 amount of non-detector material required to support the solenoid. The return yoke of the magnet
689 is provided by the iron absorber of the TileCal [41].

690 The central ATLAS toroid magnet, providing the magnetic field for the barrel region of the MS,
691 is the largest toroidal magnet ever constructed at 25 m in length. The toroid is composed of eight
692 individual coils, each housed in their own cryostat. The toroidal magnetic field is advantageous
693 as the direction of the field is almost perpendicular to the path of the charged particles. 56 km of
694 aluminum stabilized niobium-titanium-copper superconductor wire compose the magnet. In each
695 end-cap, eight smaller superconducting coils extend the toroidal magnetic field to particles leaving
696 the detector in the forward direction [41]. Figure 4.9 shows the layout of the toroid magnets.

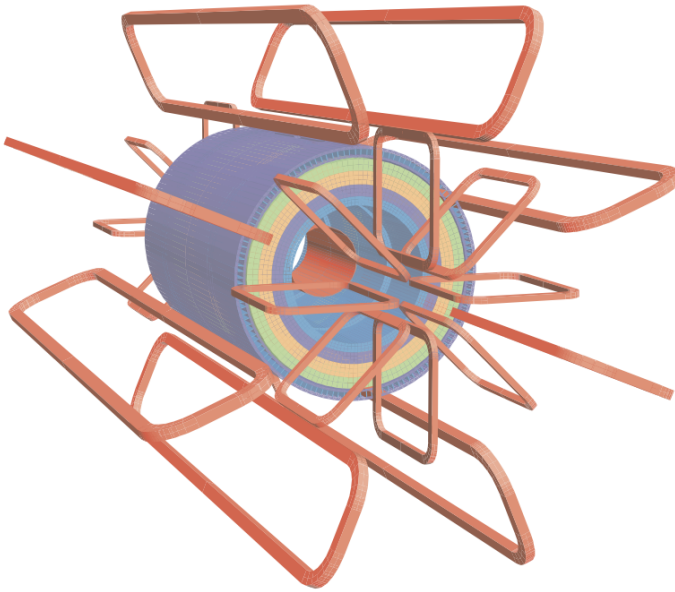


Figure 4.9: Layout of the barrel and endcap toroid magnets [32]

697 4.6 Forward Detectors

698 In addition to the inner detector, calorimeters, and muon spectrometer, three smaller detectors
699 provide coverage in the very forward region. The innermost forward detector, at 17 m from the
700 interaction point, is the **L**Uminosity measurement using **C**erenkov **I**ntegrating **D**etector (LUCID).
701 LUCID's primary purpose is to measure the relative online-luminosity for the ATLAS detector,
702 from inelastic $p - p$ scattering. The detector is composed of 20 aluminum Cerenkov tubes which
703 surround the beam pipe and face towards the interaction point.

704 The second forward detector is the Zero-Degree Calorimeter (ZDC), located 140 m from the
705 interaction point in both directions, at the point where the LHC beam-pipe divides into two separate
706 pipes. The ZDC's primary purpose is to detect forward neutrons from heavy ion collisions.

707 The third forward detector is the Absolute Luminosity For ATLAS (ALFA) system, located 240
708 m from the interaction point in both directions. ALFA determines luminosity by measuring elastic
709 scattering at small angles, from which luminosity can be calculated via the optical theorem. The
710 detector is built from scintillating fiber trackers. These are connected to the accelerator vacuum

711 via Roman pots, which allow the detector to come as close as 1mm to the beam without disrupting
712 the machine vacuum. The LUCID and ALFA detectors are crucial to determining the real-time
713 conditions of the beams and the total luminosity delivered to the ATLAS detector [32].

714 **4.7 Trigger and Data Acquisition**

715 The trigger and Data Acquisition systems (TDAQ) are responsible for selecting the most viable
716 events to save for further downstream processing. Because of the high luminosities delivered to
717 the ATLAS detector, not all events recorded can be saved; the 40 MHz bunch crossing rate must
718 be reduced by 5 orders of magnitude to an event storage rate of \sim 1 kHz. The trigger system is
719 composed of three distinct levels: Level 1 (L1), Level 2 (L2) and the event filter. Collectively the
720 L2 trigger and the event filter form the High Level Trigger (HLT).

721 The L1 trigger is implemented in the hardware of the ATLAS calorimeter and muon systems.
722 The primary modality of the L1 trigger is to identify muons, electrons, photons, jets, and τ -leptons
723 with high transverse momentum. Particles with high transverse momentum are more likely to
724 originate from direct, high energy collisions, which are most likely to produce interesting physics
725 processes. The L1 trigger also identifies events with large missing transverse energy, which could
726 be indicative of new physics. The L1 muon trigger (L1Muon) relies on RPC and TGC trigger
727 chambers in the barrel and end-cap regions of the muon spectrometer. The L1 Calorimeter Trigger
728 (L1Calo) uses reduced granularity information collected by all the calorimeter subsystems. Results
729 from the L1Muon and L1Calo triggers are combined by the Central Trigger Processor (CTP),
730 which implements a trigger ‘menu’, listing various combinations of trigger requirements. The
731 maximum L1 acceptance rate is 75 kHz, and the L1 trigger decision must reach the front-end
732 electronics within $2.5 \mu\text{s}$ of its associated bunch-crossing [32].

733 The L1 trigger defines a Region-of-Interest (RoI) for each passing event. The ROI is repre-
734 sented by the η - ϕ detector region where interesting features were identified by the L1 selection
735 process. Information about the type of feature identified and the threshold which was exceeded to
736 trigger the L1 response is also recorded. The ROI data is sent to the L2 trigger, which uses all of

737 the available information within the ROI at full granularity and precision. The L2 trigger reduces
738 the event rate from 75 kHz to 3.5 kHz, with an average processing time of 40 ms. The final stage of
739 the HLT is the event filter, which reduces the event rate to 200 Hz. The event filter uses an offline
740 analysis process to select fully rebuilt events which will be saved for further analysis.

741 All levels of the ATLAS trigger system depend on specialized electronics. Each detector front-
742 end system has a specialized Readout Driver (ROD) which collects information from several front-
743 end data streams at once. The ROD is composed of front-end analogue processing, an L1 buffer
744 which retains the information long enough for the L1 trigger decision, and dedicated links which
745 send the front-end L1 triggered data to Data Acquisition System (DAQ). Any digital signals are
746 formatted as raw data before being transferred to the DAQ. The first stage of the DAQ temporarily
747 stores the L1 data in local buffers. The ROI data is then requested by the L2 trigger, after which
748 selected events are transferred to an event building system, before events passing the event filter
749 are sent to the CERN computer center for permanent storage. The DAQ system not only allows
750 for the readout of detector data, but is also responsible for the monitoring and configuration of
751 the hardware and software components which make up the data readout system via the Detector
752 Control System (DCS).

753 The DCS allows centralized control of all detector subsystems simultaneously. It continually
754 monitors operational conditions, reports any abnormal behavior to the operator, and can perform
755 both automatic and manual interventions. The DCS reports on real time detector conditions such
756 as high or low voltage detector electronics, gas and cooling systems, magnetic field conditions,
757 humidity and temperature. This information is continually monitored by experts in the ATLAS
758 control room, so that action can be taken immediately to correct any issues that arise. The DCS also
759 handles communication between detector systems, and other systems such as the LHC accelerator,
760 the ATLAS magnets, and CERN technical services [32].

Chapter 5: Particle Reconstruction and Identification

763 With a design luminosity of $1.0 \times 10^{34} \text{ cm}^{-2}\text{s}^{-1}$, and a peak Run-2 instantaneous luminosity of
 764 $2.0 \times 10^{34} \text{ cm}^{-2}\text{s}^{-1}$, reconstructing and identifying the products of LHC $p p$ collisions is one of the
 765 most complex tasks for each LHC experiment. The accurate reconstruction and identification of
 766 physics objects lays the ground work for all subsequent physics analyses, so it is also one of the
 767 most fundamentally important tasks performed by an experiment.

768 Reconstruction is the process of combining raw and uncalibrated hits across various subsystems
 769 into specific unique objects. Two particular subsystems, the Inner Detector (ID) tracker and the
 770 calorimeters play particularly important roles and will be discussed in detail. Analysis of the
 771 properties of the reconstructed objects identifies them as photon, electrons, muons, or jets. While
 772 photons, electrons, and muons are fundamental particles, jets represent a collimated shower of
 773 many hadronic particles, whose definition is more flexible. Jet reconstruction, clustering and track
 774 association are all of particular import to jet identification, and to the later content of this thesis.
 775 Finally, reconstruction also identifies missing transverse energy E_T^{miss} in events, which is a crucial
 776 variable for BSM physics searches. Figure 5.1 shows how the physics objects listed here interact
 777 with various systems in the ATLAS detector.

778 5.1 Inner Detector Tracks

779 As the inner most layer of the detector, the ID measures charged particles close to the interac-
 780 tion point. The various hits of these charged particles throughout the ID are used to reconstruct
 781 *tracks* which give the trajectories of charged particles [43]. Track reconstruction begins by clus-
 782 tering hits in the Pixel and SCT detectors, and combining clusters from different radial layers of
 783 these detectors. The multi-layer clusters form track *seeds*, which provide initial estimates of mea-

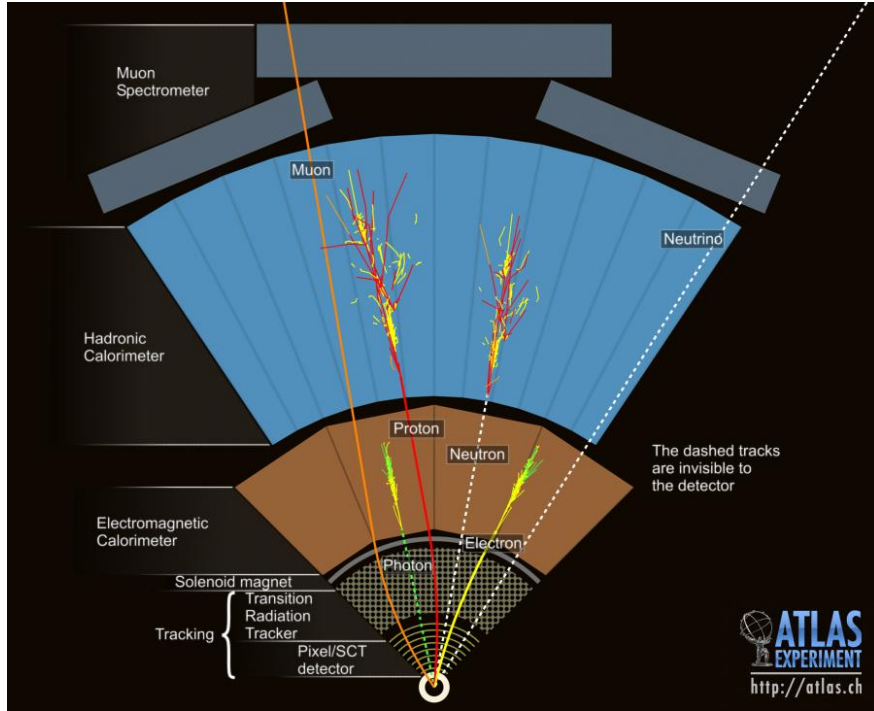


Figure 5.1: Graphic illustrating the various objects and high level features identified by ATLAS object reconstruction, and their interaction with different systems of the ATLAS detector [42]

784 surements belonging to an individual track. The requirement of three points allows for a rough
 785 estimate of the track p_T to be made by calculating the curvature of the track and accounting of the
 786 magnetic field in the ID.

787 Track seeds are subject to a variety of quality requirements, such as having a minimum esti-
 788 mated p_T and passing interaction region compatibility criterion. If these requirements are satisfied,
 789 the track seeds are passed to the track finding and fitting algorithms. The interplay of these three
 790 track reconstruction steps is illustrated in Figure 5.2.

791 **5.2 Photons and Electrons**

792 Photons and electrons shower in the LAr calorimeter, and are identified by the energy deposits
 793 they leave there. Energy deposits in a collection of nearby cells are termed *clusters*, which become
 794 the starting point for electron and photon reconstruction [44]. The clustering algorithm begins
 795 when the energy deposit in a certain cell exceeds the noise threshold with a significance of 4σ .

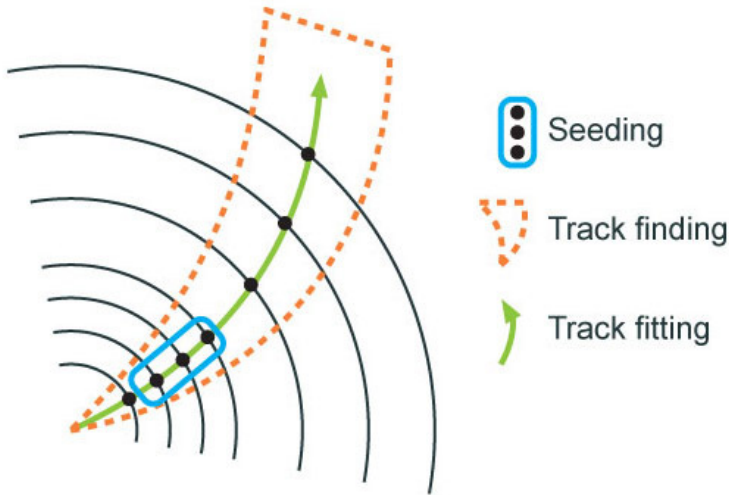


Figure 5.2: Track reconstruction seeding, finding and fitting illustration [43]

796 The algorithm then collects neighboring cells which have an energy deposit exceeding the noise
 797 threshold with a significance of 2σ , creating a topo-cluster. Next, these topo-clusters are matched
 798 to ID tracks, created as described in Section 5.1. The location of the topo-cluster defines a region
 799 of interest (ROI) in the ID, where additional modified track reconstruction algorithms are run in the
 800 case that no associated tracks are found. Any ID tracks associated to the topo-cluster are retrofitted to
 801 allow for additional energy loss due to bremsstrahlung. A converted photon track reconstruction
 802 algorithm is run to check for tracks coming from secondary vertices consistent with converted
 803 photons. The secondary vertices are constructed from two oppositely charged tracks consistent
 804 with a massless particle, or from one track without any hits in the innermost layer of the ID.

805 For electron identification, the EM cluster is required to match ID tracks that originate from
 806 the primary vertex at the interaction point. For photon identification, the EM cluster can either be
 807 matched to tracks coming from a secondary vertex (converted photon), or matched to no tracks
 808 (unconverted photon). Figure 5.3 illustrates these three cases for EM object identification.

809 *Superclusters* are built separately for photons and electrons, based on the combined topo-cluster
 810 and ID track information. First, the EM topo-clusters are tested to see if they meet the minimum
 811 requirements to become electron or photon seed clusters. For electrons, the cluster must have a
 812 minimum E_T of 1 GeV, and must be matched to a track with at least 4 hits in the silicon tracking

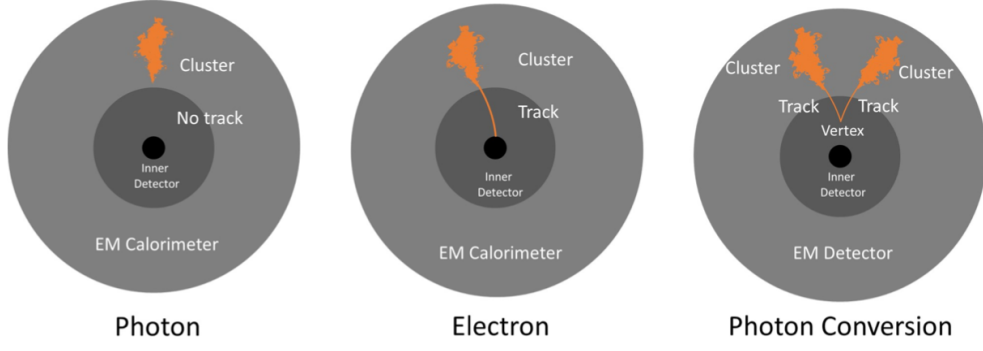


Figure 5.3: Three types of EM object candidates [45].

detectors. For photons, the cluster must have an E_T greater than 1.5 GeV. If the seed cluster requirements are met, the algorithm searches for satellite clusters, which can arise from bremsstrahlung radiation. If the satellite clusters pass the positional, energy and tracking requirements to be associated with the proto-cluster, they are combined into a supercluster.

Electron and photon objects are identified from the superclusters after energy calibration and position corrections are applied. Because photon and electron superclusters are built independently, some clusters can produce both a photon and an electron. In this case an ambiguity resolution procedure is applied to determine if the supercluster can be easily identified as only a photon (no tracks present) or only an electron (good tracks pointing to the primary vertex). In some cases, the identity of the cluster is still ambiguous, in which case both a photon and electron object are created for analysis and flagged as ambiguous. Energy, shower shape, and other analysis variables are calculated from the supercluster and saved with the electron or photon object.

5.3 Muons

Muons are identified through the tracks and energy deposits they leave in the ID, calorimeters, and Muon Spectrometer (MS). Muon identification begins in the Muon Drift Tube chambers by performing a straight line fit between the hits found in each layer, creating *segments*. Segments in the middle layers are then used as seeds for the track building algorithm, which searches for compatible combinations of segments based on their relative positions and angles [46]. A χ^2 fit is

831 performed on each track candidate. Based on the χ^2 criteria, hits are removed or added such that
832 the track contains as many hits as possible while satisfying the fit criteria.

833 The MS track candidates are combined with track information from the ID and calorimeters
834 according to various algorithms based on the information available from each subdetector. Four
835 different types of muons arise from the various reconstruction algorithms:

- 836 • Combined muon: a muon track identified through independent track reconstruction in the
837 ID and MS, where the combined track is formed using a global refit that uses hit information
838 from both detectors. Most muons are constructed through an outside-in procedure, in which
839 a muon track candidate is identified in the MS and then an associated track is found in the ID.
840 A complementary inside-out procedure is also implemented and identifies additional muons.
- 841 • Segment-tagged muon: an ID track is identified as a muon if when extrapolated out to the
842 MS (following the inside-out global fit procedure) it is matched to at least one local MS
843 segment.
- 844 • Calorimeter-tagged muon: an ID track is identified as a muon if it is matched to a calorimeter
845 energy deposit that is compatible with a minimum-ionizing particle. This muon identification
846 has the lowest purity, but it used in regions where the MS has only partial coverage due
847 to cabling and service access routes.
- 848 • Extrapolated muons: the muon is reconstruction only from the MS track and a requirement
849 on compatibility with the primary interaction point. The muon track is required to cross at
850 least two layers of the MS, and three layers in the forward region. These muons are mainly
851 used to extend muon acceptance into the region $2.5 < |\eta| < 2.7$ where ID track information
852 is not available.

853 Figure 5.4 illustrates the four types of muon reconstruction. Overlap between reconstructed
854 muons using ID tracks is resolved by giving preference to combined muons, then segment tagged
855 muons, and finally calorimeter tagged muons. Overlap with extrapolated muons is resolved by
856 giving preference to the muon with a better fit quality and higher number of tracks.

857 All muon track candidates are required to pass a series of quality selections to be identified in
 858 the final muon collection. The primary qualities considered are the χ^2 goodness of fit for the global
 859 track, the difference in p_T measurement between the ID and MS tracks, and the ratio between the
 860 charge and momentum of the tracks. The quality requirements help reject hadrons, primarily from
 861 kaon and pion decays. Muons candidates consistent with cosmic rays are also rejected.

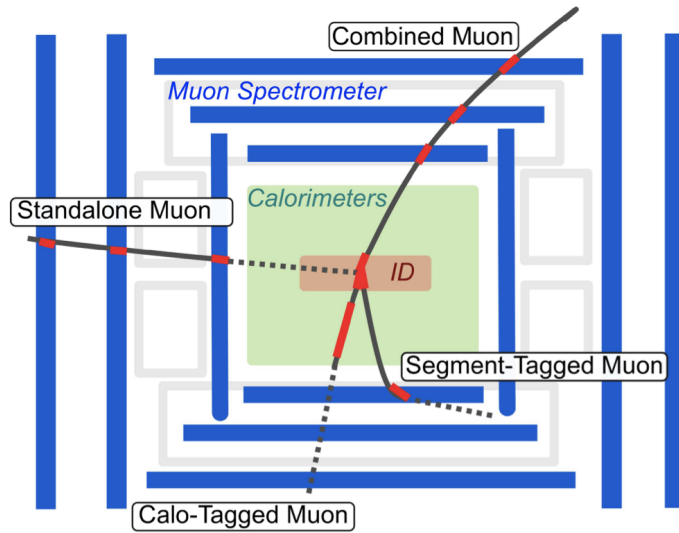


Figure 5.4: Four types of muon track candidates [47].

862 5.4 Jets

863 The protons accelerated in the LHC are composed of quarks and gluons, and thus their colli-
 864 sions often result in the release of energetic quarks and gluons, collectively termed *partons*. The
 865 energetic partons can radiate additional gluons, and these gluons can pair produce quarks in a pro-
 866 cess called *fragmentation*. Fragmentation continues until the energy drops sufficiently that color
 867 conservation plays a dominant role. At that point, additional quarks and gluons are produced from
 868 vacuum to create neutral color states for the fragmented collection of partons. This process is
 869 known as *hadronization* [48]. The hadronized partons compose a collimated stream of particles,
 870 known as a *jet*, which is then observed in the detector. The full process that produces jets is known
 871 as a *parton shower*, and is illustrated in Figure 5.5.

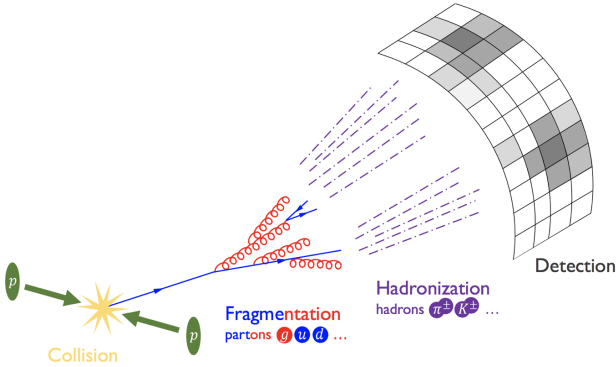


Figure 5.5: The fragmentation and hadronization processes undergone by a quark produced in a proton-proton collision [49].

872 Jets are identified by the energy deposits they leave in the calorimeter, which are then matched
 873 to the tracks they leave in the ID. Jet reconstruction generally begins in the calorimeters, with the
 874 identification of *topo-clusters*. Then jet reconstruction algorithms combine calorimeter informa-
 875 tion with tracking information. The anti- k_t algorithm [50] as provided by the FastJet library [51] is
 876 generally used by the ATLAS experiment, with varying reconstruction radius settings. There are a
 877 variety of jet collections depending on the exact usage of calorimeter and tracking information in
 878 the reconstruction. Some common collections include particle flow jets (PFlow), track calo-cluster
 879 jets (TCC), EM topo-cluster jets (EMTopo), and unified flow object jets (UFO). Only particle flow
 880 jets will be discussed in greater detail due to their importance in this analysis. The following sec-
 881 tions discuss jet identification in the calorimeters, particle flow jet construction using the anti- k_t
 882 algorithm, jet clustering and jet substructure characteristics.

883 5.4.1 Calorimeter Clusters

884 Jets are first identified by the energy deposits they leave in the calorimeters. The reconstruc-
 885 tion of jets in ATLAS begins with the construction of *topo-clusters*, which are topologically-grouped
 886 noise-suppressed clusters of calorimeter cells [52]. The topo-cluster seed is a cell with an energy
 887 that is at least 4× the average background noise level for the cell. Any cells adjacent to the seed
 888 cell in three dimensions are added to the cluster if they have an energy deposit that is at least 2x

889 the average expected noise. This process is repeated, growing the cluster, until no adjacent cells
890 exceeding the energy deposit threshold remain. As a final step, all adjacent cells are added to the
891 topo-cluster, irrespective of their energy.

892 The construction process for topo-clusters allows for the possibility that several independent
893 signatures are grouped into one topo-cluster. To correct for this, the topo-cluster is scanned for
894 local maximum, defined by any cell with energy > 500 MeV, and no neighboring cells with greater
895 energy. If more than one local maximum is identified, the topo-cluster is split among the corre-
896 sponding energy peaks [53]. In the event that one cell neighbors two or more local maxima, the
897 cell is assigned to the two highest-energy clusters that is neighbors. This means each cell is shared
898 at most once, between at most two post-splitting topo-clusters.

899 Two measurements for the total energy of the topo-cluster are considered. The raw, or electro-
900 magnetic (EM), scale simply considers the sum of energy from all cells in the topo-cluster. The
901 local cell weighting (LCW) scale first classifies clusters as electromagnetic or hadronic, and then
902 applies appropriate corrections for hadronic interactions in the jet energy calculation [52]. The
903 corrections are derived from Monte Carlo simulations, and account for the weaker response of
904 ATLAS calorimeters to hadronic interactions (ATLAS calorimeters are *non-compensating*), and
905 hadronic energy losses due to interactions with dead material [53].

906 5.4.2 Particle Flow Algorithm

907 The calorimeters provide excellent jet energy resolution for high energy jets. However, the
908 granularity of the hadronic calorimeter is restricted to 0.1×0.1 in $\eta \times \phi$. Combining the infor-
909 mation from the calorimeter with tracking information provides superior angular resolution and
910 energy resolution. The particle flow (PFlow) algorithm is one of a handful of algorithms which
911 can perform this task.

912 An overview of the process is given in Figure 5.6. Tracks from the ID which are selected for the
913 PFlow algorithm are required to have at least 9 hits in the silicon detector, and missing pixel hits in
914 places where a hit would be expected. Additionally, the tracks have $p_T > 0.5$ GeV, and $|\eta| < 2.5$.

915 The algorithm then attempts to match these tracks to EM scale calorimeter topo-clusters. This
916 matching is performed using the distance metric

$$\Delta R' = \sqrt{\left(\frac{\Delta\phi}{\sigma_\phi}\right)^2 + \left(\frac{\Delta\eta}{\sigma_\eta}\right)^2} \quad (5.1)$$

917 where σ_η and σ_ϕ represent the angular widths of the topo-clusters, and $\Delta\eta$ and $\Delta\phi$ represent the
918 distance between the track, extrapolated to the second layer of the EM calorimeter, and barycenter
919 of the topo-cluster [54]. The topo-cluster closest to the track as measured by $\Delta R'$ is considered
920 matched to the track. If no topo-cluster is found within the cone size of $\Delta R' = 1.64$, it is assumed
921 that particle which left the track did not form a topo-cluster in the calorimeter.

922 The PFlow algorithm predicts the expected single topo-cluster energy for a given track, based
923 on the track momentum and topo-cluster position. This value is then compared to the observed
924 energy of the topo-cluster, and the probability that the particle energy was deposited in more than
925 one topo-cluster is evaluated. If necessary, the algorithm adds more topo-clusters to the track/topo-
926 cluster system, in order to account of the full shower energy of the track particle.

927 To reduce the impact of double counting the energy of a given particle by including both its
928 tracker and calorimeter energy measurements, the calorimeter energy measurements associated to a
929 given track are subtracted from the total calorimeter measurement. If the expected energy deposited
930 by the particle exceeds the topo-cluster energy, the full topo-cluster is removed. If the expected
931 energy is less than the EM scale energy of all the considered topo-clusters, topo-cluster cells are
932 removed one by one, until the full expected energy deposit of the particle has been removed from
933 the calorimeter information. The resulting set of tracks and topo-clusters represent the event with
934 no double-counting of energy between subdetectors [54]. This information is passed to the jet-
935 finding algorithm.

936 5.4.3 Jet Clustering

937 When a parton decays in the detector, its energy deposits often result in multiple calorimeter
938 clusters. For physics purposes, it is useful to combine clusters that likely resulted from an individ-

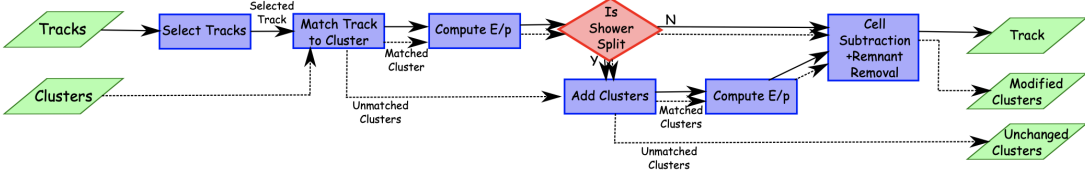


Figure 5.6: A flow chart illustrating the particle flow algorithm progression [54].

939 ual parton decay, in order to reconstruct the parton. The process of grouping topo-clusters which
 940 were produced by the same parton decay is *jet clustering*.

941 The anti- k_t algorithm is the most commonly used algorithm for jet clustering in ATLAS. The
 942 anti- k_t algorithm is based on sequential recombination algorithms [55]. A sequential recombina-
 943 tion considers the distance d_{ij} between objects i and j (particles or pseudojets), and the distance
 944 d_{iB} between an object i and the beam line B . If d_{ij} between two objects is the smallest distance
 945 among those considered, i and j are combined into a pseudojet. The process continues until the
 946 smallest distance is d_{iB} at which point the object i is determined to be a jet and removed from the
 947 objects in consideration. The procedure is repeated with the remaining objects until there are none
 948 remaining [50].

949 The anti- k_t algorithm adopts this procedure, but modifies the distance measurements d_{ij} and
 950 d_{iB} to consider the transverse momentum k_t :

$$d_{ij} = \min(k_{ti}^{2p}, k_{tj}^{2p}) \frac{\Delta_{ij}^2}{R^2}, \quad (5.2a)$$

$$d_{iB} = k_{ti}^{2p}. \quad (5.2b)$$

951 The addition of the term p allows adjustments to algorithm which govern the relative power of
 952 the momentum versus the geometrical scale $\Delta_{i,j}$, which is defined as $\Delta_{i,j} = (y_i - y_j)^2 + (\phi_i - \phi_j)^2$
 953 where y_i and ϕ_i are respectively the rapidity and azimuth of particle i [50]. The radius parameter
 954 R is chosen and determines the geometric cone size [55].

955 In the case $p = 1$ the inclusive k_t algorithm [55] is recovered, which is a standard sequential

combination jet clustering algorithm. In the case $p = 0$, the Cambridge/Aachen sequential combination algorithm [56] is recovered. The case $p = -1$ gives rise to the anti- k_t algorithm. The impact of this choice means that the distance d_{ij} between many soft particles is larger than between soft and hard particles. Therefore, soft particles tend to cluster with hard ones before they cluster with other soft particles. They key feature of this behavior is that soft particles do not modify the shape of the jets. This leads to the creation of circular conical jets, a desirable feature which sequential combination algorithms and cone algorithms struggle to achieve. Figure 5.7 compares anti- k_t jet formation with the inclusive k_t and Cambridge/Aachen algorithms mentioned here, as well as the SIScone algorithm [57], which checks for sets of stable cones compatible with the observed radiation.

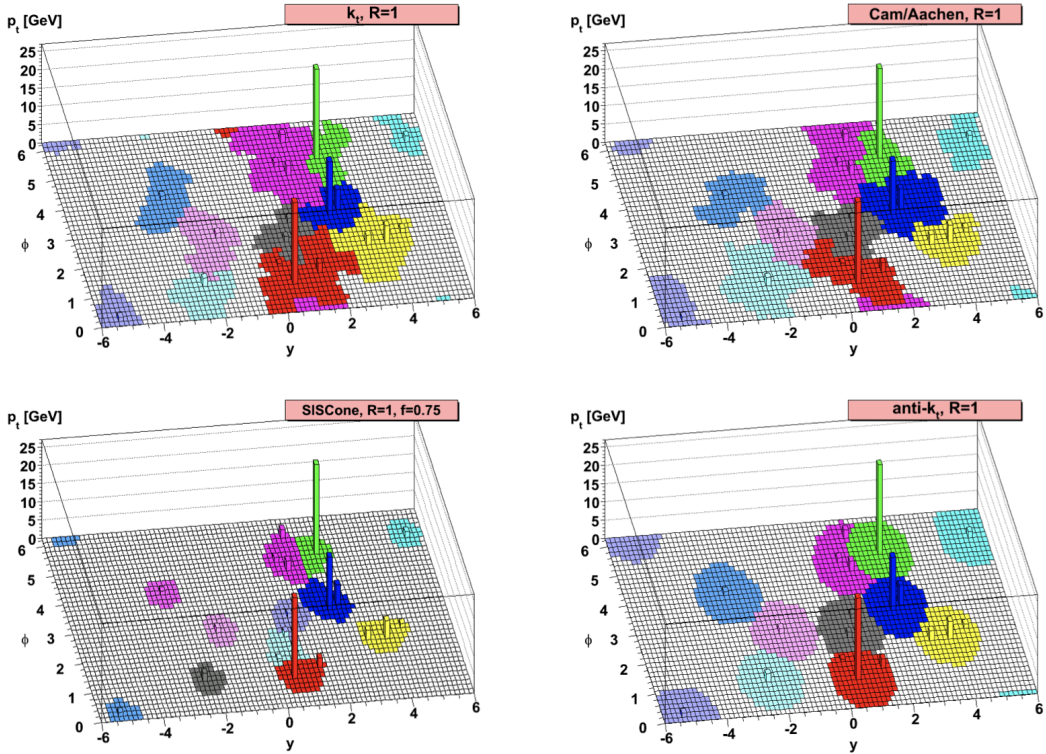


Figure 5.7: A comparison of jet clustering with four different jet algorithms. The anti- k_t algorithm is observed to create the most conical jets, where the shape of the jet is immune to the presence of soft radiation [50].

Any useful jet clustering algorithm must satisfy the requirements of infrared safety and collinear

967 (IRC) safety. Infrared safety implies that the resulting set of jets is unaltered by the presence of
968 additional soft particles in the list of seed clusters. As explained above, the anti- k_t algorithm is
969 natural infrared safe. Collinear safety requires that the final set of jets is not impacted by collinear
970 splitting of one of the jets. If the hardest particle p_1 is split into a collinear pair (p_{1a}, p_{1b}) (as
971 is common in the fragmentation process for a hard parton), the jet clustering algorithm must
972 still recognize (p_{1a}, p_{1b}) as the hardest jet in the collision. If another softer particle p_2 with
973 $p_{t,1a}, p_{t,1b} < p_{t,2} < p_{t,1}$ is instead considered the hardest particle in the event, a different final
974 set of jets would be returned. Collinear safety is a requirement of perturbative QCD, to ensure
975 non-divergent higher-order calculations [58]. The anti- k_t algorithm's tendency to cluster hard par-
976 ticles first ensures its collinear safety. By satisfying the IRC safety requirement, anti- k_t jets can be
977 calculated using perturbative QCD, which improves comparisons with theory.

978 5.4.4 Ghost Track Association

979 Once a collection of jets has been created, the jet objects can be studied at both the event-level
980 and the jet-level. In the event-level picture, the momentum, energy, and geometric orientation
981 of the jets within an event are considered. This yields important information about decay of any
982 resonant heavy objects, the total energy in the event, and the distribution of energy amongst the jets.
983 At the jet-level picture, the particles composing the jet are considered. The momentum, energy,
984 and geometric orientation of the particle tracks provides a low-level picture of the jet, which can
985 help determine if the properties of the jet are consistent with standard QCD, or if new physics
986 processes might be represented within the patterns found in the constituent particles. Jet-level
987 analysis is also widely used in flavor tagging.

988 For anti- k_t jets with a radius parameter $R = 0.4$, one way of studying the jet-level picture
989 is through considering the ghost-associated tracks. Track association is process of determining
990 which tracks should be considered associated with a given jet. In the ghost association algorithm,
991 the anti- k_t clustering algorithm is used for the collection of tracks and calorimeter clusters [59].
992 However, the tracks are considered to have infinitesimal momentum (*ghosts*), so their addition to

993 a jet object does not alter the four-momentum of the jet. This ensures the final jet collection is not
994 altered by the presence of the ghost tracks in the reclustering, but information about the associated
995 tracks for each reconstructed jet becomes available [60].

996 Ghost tracks are of particular importance to this analysis, as a means of providing a low-level
997 picture of the shape of $R = 0.4$ jets, and discriminating Standard Model QCD-like jets from dark
998 QCD-like jets.

999 5.5 Missing Transverse Energy

1000 A simple principle leveraged in ATLAS physics analyses is checking for conservation of mo-
1001 mentum among the products of any pp collisions. The initial state transverse momentum of any
1002 pp collision is always zero, so the transverse momentum of all final state particles should likewise
1003 be zero. The missing transverse energy, E_T^{miss} , is determined by the magnitude of the negative
1004 momentum vector sum of all final state objects resulting from the pp collision.

1005 Specifically, the objects considered in the E_T^{miss} calculation are photons, electrons, muons, jets,
1006 and soft terms. The first four items comprise the hard components of the E_T^{miss} calculation, and
1007 have been discussed previously in this chapter. The final item represents a collection of *soft terms*,
1008 comprising any detector signals not associated to hard detector objects. These can be based on
1009 unassociated tracks, or unassociated soft calorimeter clusters. Both are generally not used in the
1010 same calculation to avoid double counting of soft terms. In this analysis the calorimeter cluster
1011 soft terms are considered in the E_T^{miss} calculation.

1012 E_T^{miss} can arise due to non-interacting Standard Model objects such as neutrinos, fake sources
1013 such as mis-reconstructed objects and dead detector regions, or in some theories, non-interacting
1014 BSM objects such as a dark matter candidate particles. To understand the amount of E_T^{miss} at-
1015 tributable to detector noise and mis-reconstruction, E_T^{miss} is studied in $Z \rightarrow \mu\mu$ where little real
1016 E_T^{miss} is expected [61]. As Figure 5.8 illustrates, the resolution of E_T^{miss} generally decreases as
1017 E_T^{miss} increases, due to detector resolution effects. As E_T^{miss} is an important quantity for most dark
1018 QCD analyses, limitations in the accuracy of the E_T^{miss} calculation must be considered.

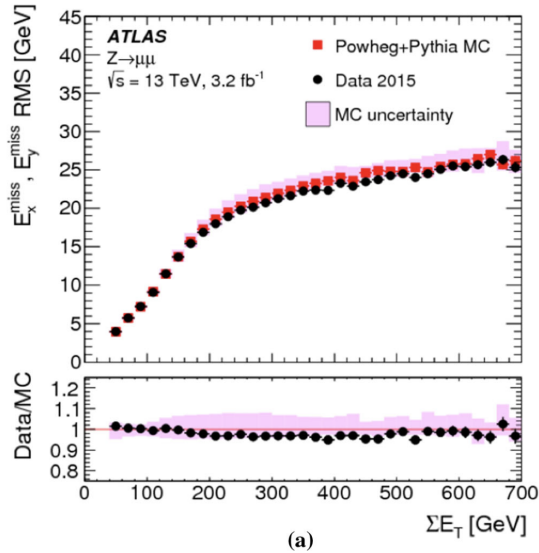


Figure 5.8: A comparison of MC simulation and data for $Z \rightarrow \mu\mu$ events where real $E_T^{\text{miss}} = 0$ [61]. The resolution of the missing energy in the transverse ($x - y$) plane is observed to increase with increasing total $\sum E_T$.

1019

Conclusion or Epilogue

1020 Use this page for your epilogue or conclusion if applicable; please use only one of the titles
1021 for this page. Otherwise, you may delete it. Use this page for your epilogue or conclusion if
1022 applicable; please use only one of the titles for this page. Otherwise, you may delete it. Use this
1023 page for your epilogue or conclusion if applicable; please use only one of the titles for this page.
1024 Otherwise, you may delete it. Use this page for your epilogue or conclusion if applicable; please
1025 use only one of the titles for this page. Otherwise, you may delete it. Use this page for your
1026 epilogue or conclusion if applicable; please use only one of the titles for this page. Otherwise,
1027 you may delete it. Use this page for your epilogue or conclusion if applicable; please use only one
1028 of the titles for this page. Otherwise, you may delete it. Use this page for your epilogue or
1029 conclusion if applicable; please use only one of the titles for this page. Otherwise, you may delete
1030 it. Use this page for your epilogue or conclusion if applicable; please use only one of the titles for
1031 this page. Otherwise, you may delete it. Use this page for your epilogue or conclusion if
1032 applicable; please use only one of the titles for this page. Otherwise, you may delete it. Use this
1033 page for your epilogue or conclusion if applicable; please use only one of the titles for this page.
1034 Otherwise, you may delete it. Use this page for your epilogue or conclusion if applicable; please
1035 use only one of the titles for this page. Otherwise, you may delete it. Use this page for your
1036 epilogue or conclusion if applicable; please use only one of the titles for this page. Otherwise,
1037 you may delete it. Use this page for your epilogue or conclusion if applicable; please use only one
1038 of the titles for this page. Otherwise, you may delete it. Use this page for your epilogue or
1039 conclusion if applicable; please use only one of the titles for this page. Otherwise, you may delete

1040 it. Use this page for your epilogue or conclusion if applicable; please use only one of the titles for
1041 this page. Otherwise, you may delete it. Use this page for your epilogue or conclusion if
1042 applicable; please use only one of the titles for this page. Otherwise, you may delete it. Use this
1043 page for your epilogue or conclusion if applicable; please use only one of the titles for this page.
1044 Otherwise, you may delete it. Use this page for your epilogue or conclusion if applicable; please
1045 use only one of the titles for this page. Otherwise, you may delete it. Use this page for your
1046 epilogue or conclusion if applicable; please use only one of the titles for this page. Otherwise,
1047 you may delete it. Use this page for your epilogue or conclusion if applicable; please use only one
1048 of the titles for this page. Otherwise, you may delete it. Use this page for your epilogue or
1049 conclusion if applicable; please use only one of the titles for this page. Otherwise, you may delete
1050 it. Use this page for your epilogue or conclusion if applicable; please use only one of the titles for
1051 this page. Otherwise, you may delete it. Use this page for your epilogue or conclusion if
1052 applicable; please use only one of the titles for this page. Otherwise, you may delete it. Use this
1053 page for your epilogue or conclusion if applicable; please use only one of the titles for this page.
1054 Otherwise, you may delete it. Use this page for your epilogue or conclusion if applicable; please
1055 use only one of the titles for this page. Otherwise, you may delete it. Use this page for your
1056 epilogue or conclusion if applicable; please use only one of the titles for this page. Otherwise,
1057 you may delete it. Use this page for your epilogue or conclusion if applicable; please use only one
1058 of the titles for this page. Otherwise, you may delete it. Use this page for your epilogue or
1059 conclusion if applicable; please use only one of the titles for this page. Otherwise, you may delete
1060 it. Use this page for your epilogue or conclusion if applicable; please use only one of the titles for
1061 this page. Otherwise, you may delete it. Use this page for your epilogue or conclusion if
1062 applicable; please use only one of the titles for this page. Otherwise, you may delete it. Use this
1063 page for your epilogue or conclusion if applicable; please use only one of the titles for this page.
1064 Otherwise, you may delete it. Use this page for your epilogue or conclusion if applicable; please
1065 use only one of the titles for this page. Otherwise, you may delete it. Use this page for your
1066 epilogue or conclusion if applicable; please use only one of the titles for this page. Otherwise,

1067 you may delete it. Use this page for your epilogue or conclusion if applicable; please use only one
1068 of the titles for this page. Otherwise, you may delete it. Use this page for your epilogue or
1069 conclusion if applicable; please use only one of the titles for this page. Otherwise, you may delete
1070 it. Use this page for your epilogue or conclusion if applicable; please use only one of the titles for
1071 this page. Otherwise, you may delete it. Use this page for your epilogue or conclusion if
1072 applicable; please use only one of the titles for this page. Otherwise, you may delete it. Use this
1073 page for your epilogue or conclusion if applicable; please use only one of the titles for this page.
1074 Otherwise, you may delete it. Use this page for your epilogue or conclusion if applicable; please
1075 use only one of the titles for this page. Otherwise, you may delete it. Use this page for your
1076 epilogue or conclusion if applicable; please use only one of the titles for this page. Otherwise,
1077 you may delete it. Use this page for your epilogue or conclusion if applicable; please use only one
1078 of the titles for this page. Otherwise, you may delete it. Use this page for your epilogue or
1079 conclusion if applicable; please use only one of the titles for this page. Otherwise, you may delete
1080 it. Use this page for your epilogue or conclusion if applicable; please use only one of the titles for
1081 this page. Otherwise, you may delete it. Use this page for your epilogue or conclusion if
1082 applicable; please use only one of the titles for this page. Otherwise, you may delete it. Use this
1083 page for your epilogue or conclusion if applicable; please use only one of the titles for this page.
1084 Otherwise, you may delete it. Use this page for your epilogue or conclusion if applicable; please
1085 use only one of the titles for this page. Otherwise, you may delete it. Use this page for your
1086 epilogue or conclusion if applicable; please use only one of the titles for this page. Otherwise,
1087 you may delete it. Use this page for your epilogue or conclusion if applicable; please use only one
1088 of the titles for this page. Otherwise, you may delete it. Use this page for your epilogue or
1089 conclusion if applicable; please use only one of the titles for this page. Otherwise, you may delete
1090 it. Use this page for your epilogue or conclusion if applicable; please use only one of the titles for
1091 this page. Otherwise, you may delete it. Use this page for your epilogue or conclusion if
1092 applicable; please use only one of the titles for this page. Otherwise, you may delete it. Use this
1093 page for your epilogue or conclusion if applicable; please use only one of the titles for this page.

1094 Otherwise, you may delete it. Use this page for your epilogue or conclusion if applicable; please
1095 use only one of the titles for this page. Otherwise, you may delete it. Use this page for your
1096 epilogue or conclusion if applicable; please use only one of the titles for this page. Otherwise,
1097 you may delete it. Use this page for your epilogue or conclusion if applicable; please use only one
1098 of the titles for this page. Otherwise, you may delete it. Use this page for your epilogue or
1099 conclusion if applicable; please use only one of the titles for this page. Otherwise, you may delete
1100 it. Use this page for your epilogue or conclusion if applicable; please use only one of the titles for
1101 this page. Otherwise, you may delete it. Use this page for your epilogue or conclusion if
1102 applicable; please use only one of the titles for this page. Otherwise, you may delete it. Use this
1103 page for your epilogue or conclusion if applicable; please use only one of the titles for this page.
1104 Otherwise, you may delete it. Use this page for your epilogue or conclusion if applicable; please
1105 use only one of the titles for this page. Otherwise, you may delete it. Use this page for your
1106 epilogue or conclusion if applicable; please use only one of the titles for this page. Otherwise,
1107 you may delete it. Use this page for your epilogue or conclusion if applicable; please use only one
1108 of the titles for this page. Otherwise, you may delete it. Use this page for your epilogue or
1109 conclusion if applicable; please use only one of the titles for this page. Otherwise, you may delete
1110 it. Use this page for your epilogue or conclusion if applicable; please use only one of the titles for
1111 this page. Otherwise, you may delete it. Use this page for your epilogue or conclusion if
1112 applicable; please use only one of the titles for this page. Otherwise, you may delete it. Use this
1113 page for your epilogue or conclusion if applicable; please use only one of the titles for this page.
1114 Otherwise, you may delete it. Use this page for your epilogue or conclusion if applicable; please
1115 use only one of the titles for this page. Otherwise, you may delete it. Use this page for your
1116 epilogue or conclusion if applicable; please use only one of the titles for this page. Otherwise,
1117 you may delete it. Use this page for your epilogue or conclusion if applicable; please use only one
1118 of the titles for this page. Otherwise, you may delete it. Use this page for your epilogue or
1119 conclusion if applicable; please use only one of the titles for this page. Otherwise, you may delete
1120 it.

References

- 1122 [1] Jens Erler and Paul Langacker. “Electroweak model and constraints on new physics”. In:
 1123 (July 2004). arXiv: hep-ph/0407097.
- 1124 [2] David J Griffiths. *Introduction to elementary particles; 2nd rev. version*. Physics textbook.
 1125 New York, NY: Wiley, 2008.
- 1126 [3] M. Tanabashi et al. “Review of Particle Physics”. In: *Phys. Rev. D* 98 (3 2018), pp. 847–851.
- 1127 [4] E. Noether. “Invariante Variationsprobleme”. In: *Nachr. d. König. Gesellsch. d. Wiss. zu
 1128 Göttingen, Math-phys. Klasse, Seite 235-157* (1918). eprint: www.physics.ucla.edu/
 1129 \~\cwp/articles/noether.trans/german/emmy235.html.
- 1130 [5] J. H. Christenson et al. “Evidence for the 2π Decay of the K_2^0 Meson”. In: *Phys. Rev. Lett.*
 1131 13 (1964), pp. 138–140.
- 1132 [6] J. E. Augustin et al. “Discovery of a Narrow Resonance in e^+e^- Annihilation”. In: *Phys.
 1133 Rev. Lett.* 33 (1974), pp. 1406–1408.
- 1134 [7] J. J. Aubert et al. “Experimental Observation of a Heavy Particle J ”. In: *Phys. Rev. Lett.* 33
 1135 (1974), pp. 1404–1406.
- 1136 [8] Martin L. Perl et al. “Evidence for Anomalous Lepton Production in e+ - e- Annihilation”.
 1137 In: *Phys. Rev. Lett.* 35 (1975), pp. 1489–1492.
- 1138 [9] S. W. Herb et al. “Observation of a Dimuon Resonance at 9.5-GeV in 400-GeV Proton-
 1139 Nucleus Collisions”. In: *Phys. Rev. Lett.* 39 (1977), pp. 252–255.
- 1140 [10] F. Abe et al. “Observation of top quark production in $\bar{p}p$ collisions”. In: *Phys. Rev. Lett.* 74
 1141 (1995), pp. 2626–2631. arXiv: hep-ex/9503002.
- 1142 [11] S. Abachi et al. “Observation of the top quark”. In: *Phys. Rev. Lett.* 74 (1995), pp. 2632–
 1143 2637. arXiv: hep-ex/9503003.
- 1144 [12] K. Kodama et al. “Observation of tau neutrino interactions”. In: *Phys. Lett. B* 504 (2001),
 1145 pp. 218–224. arXiv: hep-ex/0012035.
- 1146 [13] G. Arnison et al. “Experimental Observation of Lepton Pairs of Invariant Mass Around 95-
 1147 GeV/c**2 at the CERN SPS Collider”. In: *Phys. Lett. B* 126 (1983), pp. 398–410.

- 1148 [14] P. Bagnaia et al. “Evidence for $Z^0 \rightarrow e^+e^-$ at the CERN $\bar{p}p$ Collider”. In: *Phys. Lett. B* 129
 1149 (1983), pp. 130–140.
- 1150 [15] Serguei Chatrchyan et al. “Observation of a New Boson at a Mass of 125 GeV with the
 1151 CMS Experiment at the LHC”. In: *Phys. Lett. B* 716 (2012), pp. 30–61. arXiv: 1207.7235
 1152 [hep-ex].
- 1153 [16] Georges Aad et al. “Observation of a new particle in the search for the Standard Model
 1154 Higgs boson with the ATLAS detector at the LHC”. In: *Phys. Lett. B* 716 (2012), pp. 1–29.
 1155 arXiv: 1207.7214 [hep-ex].
- 1156 [17] K. G. Begeman, A. H. Broeils, and R. H. Sanders. “Extended rotation curves of spiral galaxies:
 1157 Dark haloes and modified dynamics”. In: *Mon. Not. Roy. Astron. Soc.* 249 (1991), p. 523.
- 1158 [18] Y. Ashie et al. “Evidence for an oscillatory signature in atmospheric neutrino oscillation”.
 1159 In: *Phys. Rev. Lett.* 93 (2004), p. 101801. arXiv: hep-ex/0404034.
- 1160 [19] C. Abel et al. “Measurement of the Permanent Electric Dipole Moment of the Neutron”. In:
 1161 *Phys. Rev. Lett.* 124.8 (2020), p. 081803. arXiv: 2001.11966 [hep-ex].
- 1162 [20] Guillaume Albouy et al. “Theory, phenomenology, and experimental avenues for dark showers:
 1163 a Snowmass 2021 report”. In: *The European Physical Journal C* 82.12 (Dec. 2022).
- 1164 [21] Lyndon Evans and Philip Bryant. “LHC Machine”. In: *Journal of Instrumentation* 3.08
 1165 (2008), S08001.
- 1166 [22] “The ATLAS Experiment at the CERN Large Hadron Collider”. In: *JINST* 3 (2008). Also
 1167 published by CERN Geneva in 2010, S08003.
- 1168 [23] “The CMS experiment at the CERN LHC”. In: *Journal of Instrumentation* 3.08 (2008),
 1169 S08004.
- 1170 [24] “The ALICE experiment at the CERN LHC”. In: *Journal of Instrumentation* 3.08 (2008),
 1171 S08002.
- 1172 [25] “The LHCb Detector at the LHC”. In: *Journal of Instrumentation* 3.08 (2008), S08005.
- 1173 [26] Ana Lopes and Melissa Loyse Perrey. *FAQ-LHC The guide*. 2022.
- 1174 [27] Esma Mobs. “The CERN accelerator complex in 2019. Complexe des accélérateurs du
 1175 CERN en 2019”. In: (2019). General Photo.
- 1176 [28] *Pulling together: Super Conducting electromagnets*. <https://home.cern/science/engineering/pulling-together-superconducting-electromagnets>.
 1177 Accessed: 2024-01-05.

- 1179 [29] *The High-Luminosity LHC*. <https://voisins.web.cern.ch/en/high-luminosity-lhc-hl-lhc>. Accessed: 2024-01-05.
- 1180
- 1181 [30] Aad G., et al. (ATLAS Collaboration and CMS Collaboration). “Combined Measurement of
1182 the Higgs Boson Mass in pp Collisions at $\sqrt{s} = 7$ and 8 TeV with the ATLAS and CMS
1183 Experiments”. In: *Phys. Rev. Lett.* 114 (19 2015), p. 191803.
- 1184 [31] O. Aberle et al. *High-Luminosity Large Hadron Collider (HL-LHC): Technical design re-*
1185 *port*. CERN Yellow Reports: Monographs. Geneva: CERN, 2020.
- 1186 [32] The ATLAS Collaboration. “The ATLAS Experiment at the CERN Large Hadron Collider”.
1187 In: *Journal of Instrumentation* 3.08 (2008), S08003.
- 1188 [33] G Aad, B Abbott, and ATLAS Collaboration. “Performance of the reconstruction of large
1189 impact parameter tracks in the inner detector of ATLAS”. In: *Eur. Phys. J. C Part. Fields*
1190 83.11 (Nov. 2023).
- 1191 [34] Joao Pequenao. *Computer Generated image of the ATLAS calorimeter*. 2008.
- 1192 [35] *ATLAS liquid-argon calorimeter: Technical Design Report*. Technical design report. AT-
1193 LAS. Geneva: CERN, 1996.
- 1194 [36] H A Gordon. “Liquid argon calorimetry for the SSC”. In: () .
- 1195 [37] Henric Wilkens and (on behalf of the ATLAS LArg Collaboration). “The ATLAS Liquid
1196 Argon calorimeter: An overview”. In: *Journal of Physics: Conference Series* 160.1 (2009),
1197 p. 012043.
- 1198 [38] *Technical Design Report for the Phase-II Upgrade of the ATLAS Tile Calorimeter*. Tech.
1199 rep. Geneva: CERN, 2017.
- 1200 [39] “Technical Design Report for the Phase-II Upgrade of the ATLAS Muon Spectrometer”. In:
1201 () .
- 1202 [40] L Pontecorvo. “The ATLAS Muon Spectrometer”. In: (2004). revised version number 1
1203 submitted on 2003-07-27 16:31:16.
- 1204 [41] *ATLAS magnet system: Technical Design Report, 1*. Technical design report. ATLAS. Geneva:
1205 CERN, 1997.
- 1206 [42] Joao Pequenao. “Event Cross Section in a computer generated image of the ATLAS detec-
1207 tor.” 2008.
- 1208 [43] ATLAS Collaboration. “ATLAS Experiment Implements Heterogeneous Particle Recon-
1209 struction with Intel oneAPI Tools”. General Photo. 2023.

- 1210 [44] ATLAS Collaboration. “Electron and photon performance measurements with the ATLAS
 1211 detector using the 2015–2017 LHC proton-proton collision data”. In: *Journal of Instrumentation*
 1212 14.12 (2019), P12006.
- 1213 [45] Chiara Deponte. “Studies on the properties of non-prompt photons at the ATLAS experi-
 1214 ment”. Presented 16 Aug 2022. Technische Universitaet Dortmund (DE), 2022.
- [46] ATLAS Collaboration. “Muon reconstruction performance of the ATLAS detector in pro-
 ton–proton collision data at
 \sqrt{s}
 1215 s = 13 TeV”. In: *The European Physical Journal C* 76.5 (2016).
- 1216 [47] Sebastien Rettie. *Muon identification and performance in the ATLAS experiment*. Tech. rep.
 1217 Geneva: CERN, 2018.
- 1218 [48] B. R. Webber. *Fragmentation and Hadronization*. 1999. arXiv: hep-ph/9912292 [hep-ph].
- 1219 [49] Eric M. Metodiev. *The Fractal Lives of Jets* | Eric M. Metodiev — ericmetodiev.com. https :
 1220 //www.ericmetodiev.com/post/jetformation/. 2019, note = [Accessed 18-
 1221 05-2024],
- 1222 [50] Matteo Cacciari, Gavin P Salam, and Gregory Soyez. “The anti-k_Tjet clustering algorithm”.
 1223 In: *Journal of High Energy Physics* 2008.04 (Apr. 2008), 063–063.
- 1224 [51] Matteo Cacciari, Gavin P. Salam, and Gregory Soyez. “FastJet user manual: (for version
 1225 3.0.2)”. In: *The European Physical Journal C* 72.3 (Mar. 2012).
- 1226 [52] Steven Schramm. *ATLAS Jet Reconstruction, Calibration, and Tagging of Lorentz-boosted
 1227 Objects*. Tech. rep. Geneva: CERN, 2017.
- 1228 [53] ATLAS Collaboration. “Topological cell clustering in the ATLAS calorimeters and its per-
 1229 formance in LHC Run 1”. In: *The European Physical Journal C* 77.7 (July 2017).
- 1230 [54] ATLAS Collaboration. “Jet reconstruction and performance using particle flow with the
 1231 ATLAS Detector”. In: *The European Physical Journal C* 77.7 (July 2017).
- 1232 [55] Stephen D. Ellis and Davison E. Soper. “Successive combination jet algorithm for hadron
 1233 collisions”. In: *Physical Review D* 48.7 (Oct. 1993), 3160–3166.
- 1234 [56] M. Wobisch and T. Wengler. *Hadronization Corrections to Jet Cross Sections in Deep-
 1235 Inelastic Scattering*. 1999. arXiv: hep-ph/9907280 [hep-ph].
- 1236 [57] Gavin P Salam and Grégory Soyez. “A practical seedless infrared-safe cone jet algorithm”.
 1237 In: *Journal of High Energy Physics* 2007.05 (May 2007), 086–086.

- 1238 [58] Gavin P. Salam. “Towards jetography”. In: *The European Physical Journal C* 67.3–4 (May
1239 2010), 637–686.
- 1240 [59] *A Monte Carlo study of track association to jets for b-tagging*. Tech. rep. Geneva: CERN,
1241 2021.
- 1242 [60] *Flavor Tagging with Track Jets in Boosted Topologies with the ATLAS Detector*. Tech. rep.
1243 All figures including auxiliary figures are available at <https://atlas.web.cern.ch/Atlas/GROUPS/PHYSICS/P>
1244 PHYS-PUB-2014-013. Geneva: CERN, 2014.
- 1245 [61] ATLAS Collaboration. “Performance of missing transverse momentum reconstruction with
1246 the ATLAS detector using proton-proton collisions at $\sqrt{s} = 13$ TeV”. In: *Eur. Phys. J. C*
1247 78.11 (2018), p. 903. arXiv: 1802 . 08168.

1248

1249

Appendix A: Experimental Equipment

1250 Lorem ipsum dolor sit amet, consectetur adipiscing elit, sed do eiusmod tempor incididunt ut
1251 labore et dolore magna aliqua. Ut enim ad minim veniam, quis nostrud exercitation ullamco laboris
1252 nisi ut aliquip ex ea commodo consequat. Duis aute irure dolor in reprehenderit in voluptate velit
1253 esse cillum dolore eu fugiat nulla pariatur. Excepteur sint occaecat cupidatat non proident, sunt in
1254 culpa qui officia deserunt mollit anim id est laborum.

1255

1256

Appendix B: Data Processing

1257 Lorem ipsum dolor sit amet, consectetur adipiscing elit, sed do eiusmod tempor incididunt ut
1258 labore et dolore magna aliqua. Ut enim ad minim veniam, quis nostrud exercitation ullamco laboris
1259 nisi ut aliquip ex ea commodo consequat. Duis aute irure dolor in reprehenderit in voluptate velit
1260 esse cillum dolore eu fugiat nulla pariatur. Excepteur sint occaecat cupidatat non proident, sunt in
1261 culpa qui officia deserunt mollit anim id est laborum.